Orientational ordering benefits nanorod sonication

Zornitza P. Tosheva and Jan P. F. Lagerwall[*,†]
University of Luxembourg, Department of Physics & Materials Science, L-1511 Luxembourg City, Luxembourg

(Received 12 May 2025; revised 7 November 2025; accepted 11 February 2026; published 9 March 2026)

While ultrasonication is a well established method to disperse nanorods, insufficient attention has been given to the impact of the particle mass fraction W_s at which sonication takes place. Its importance goes far beyond viscosity tuning, since a dilute isotropic nanorod suspension transitions to a liquid crystal (LC) phase if W_s surpasses a threshold, via a wide biphasic window of isotropic–LC equilibrium phase coexistence. By systematically varying W_s of suspensions of cellulose nanocrystals (CNCs) across and beyond the biphasic range we show that W_s strongly influences the sonication process. Near the original suspension's stability limit of the isotropic phase, W_0^*, the sonication shear flow induces a temporarily ordered paranematic state which assists particle individualization and minimizes damage. Our atomic force microscopy study supports this, finding increasing aspect ratio nanorods as W_s is increased from the fully isotropic range past the onset of the equilibrium biphasic window. W_s impacts also the macroscopic properties like the phase diagram and the pitch of the cholesteric LC helix into which CNCs self-assemble. A further key finding is that CNC suspensions concentrated beyond the threshold for gelation should be sonicated to remove end-to-end chains formed in the gel, since otherwise these remain even after dilution. Our conclusions apply also to many other nanorod, nanotube and nanoplatelet suspensions, where reproducibility problems may be due to the lack of control of W_s and to agglomerates remaining from high-concentration precursor suspensions.

DOI: 10.1103/9rny-g949

I. INTRODUCTION

Due to their notorious tendency to agglomerate, nanoparticles are typically dispersed as liquid suspensions that undergo sonication (ultrasound treatment) or other types of processing that involve strong shear flow to break up bundles [1–5], sometimes even at the synthesis stage [6]. This is particularly critical for anisometric nanoparticles with large interfacial contact area that renders bundle disruption challenging, like carbon nanotubes, organic or inorganic nanorods, flakes of nanoclay or graphene or graphene oxide, and bioderived nanorods such as amylose fibrils [7], chitin nanocrystals (ChNCs) [8,9] and cellulose nanocrystals (CNCs) [9–12]. The latter earned wide popularity as accessible, low-cost and sustainably produced nanorods with excellent mechanical and optical properties that are easy to disperse in water, enabling advanced functional materials with minimum environmental footprint. They are explored, e.g., as fillers in composites [13,14], in food packaging [15,16], and they give rise to spectacular photonic properties when dried as films [17–19], topographically modulated surfaces [20] or microparticles [21,22]. Because they are transparent, they also present an excellent model system to study the behavior of bulk nanoparticle suspensions by optical methods, which is often impossible for strongly absorbing nanoparticles like carbon nanotubes or graphene. To avoid CNC agglomeration into bundles, their suspensions are always sonicated, at least during the initial production. Many users apply further sonication of their stock suspensions prior to application.

While sonication is effective in breaking up bundles, it can also damage anisometric nanoparticles. They are typically shortened due to scission induced by strong extensional flow or following frequent collisions between randomly oriented particles during sonication of isotropic suspensions [23,24]. The impact of sonication on CNCs, their suspensions as well as on dry CNC films is well documented [2,25], generally focusing on the impact of sonication power, energy and time. Among the effects demonstrated are, e.g., variations of the photonic performance [26], variations in efficiency as lubricants [27], variations in rheological and colloidal properties [28,29], reduction in kinks along individual CNCs [30], and variations in gelation threshold [31]. Surprisingly, a parameter that has been neglected is the particle mass fraction W_s in the suspension while it is being sonicated. Most researchers select a single, arbitrarily chosen value of W_s for all experiments, while some do not mention the value of W_s. Here we demonstrate that this is a glaring omission, because W_s has strong impact through its role in determining the physical behavior of suspensions of anisometric nanoparticles before and during sonication. Variations in W_s affect the appearance of long-range orientational (nematic) order, the spontaneous separation into isotropic and liquid crystal (LC) phases coexisting in equilibrium [12], with an accompanying fractionation

[*]Contact author: jan.lagerwall@lcsoftmatter.com
[†]https://lcsoftmatter.com

Published by the American Physical Society under the terms of the Creative Commons Attribution 4.0 International license. Further distribution of this work must maintain attribution to the author(s) and the published article's title, journal citation, and DOI.

of disperse nanoparticles [32–35], and the onset of kinetic arrest with subsequent departure from equilibrium behavior [12]. The impact is not limited to CNCs but it should apply to any nanorods, nanotubes or nanoflakes that can develop nematic order in suspension, whether spontaneous or shear-induced.

Although the detailed shapes of individual CNCs vary, they can be approximated as twisted rectangular cuboids [36], with length L on the order of 100 nm and lateral dimensions (breadth B and thickness T) in the range of a few nanometers. It is this high aspect ratio that leads to the appearance of nematic order if the CNC volume fraction is high enough, as explained by the classic Onsager theory [37]: a low-concentration suspension of identical cylindrical nanorods with effective diameter D_e and effective length L_e remains uniformly isotropic only up to a critical particle volume fraction $\phi_0 = 3.3D_e/L_e$. A similar relationship holds for nanoplatelets. In contrast to Onsager's rods, CNCs are not cylindrical at the individual scale. However, the important aspect is their effective appearance in a colloidal suspension, where one must take, first, dynamics into account: nanorods may undergo thermally activated rapid rotations about the main moment of inertia. Second, the electrostatic repulsion that prevents nanorods from agglomerating adds approximately 1 nm to the effective radius and may smoothen out topographical variations of the CNC itself [38]. As a result, it is often a reasonable approximation to consider a cylindrical effective shape of the suspended nanorods, explaining why the Onsager theory is highly successful in modeling the behavior of CNC suspensions.

If the particle volume fraction ϕ increases beyond ϕ_0, a suspension enters a biphasic regime in which the isotropic phase coexists in equilibrium with nematic LC phase nucleating in so-called *tactoids* [39], with a local rod volume fraction $\phi_1 = 4.5D_e/L_e$. The biphasic regime extends until the overall suspension has a global particle volume fraction $\phi = \phi_1$. In the LC phase, the nanorods spontaneously align along a common direction $\mathbf{n}$ (the director), giving rise to birefringence with $\mathbf{n}$ as optic axis. Because cellulose is chiral, the nematic phase developed by CNC suspensions is chiral also at macroscopic scale, and we refer to it as *chiral nematic* or *cholesteric*. Its signature feature is the characteristic cholesteric rotation of $\mathbf{n}$ in a helical manner along an axis $\mathbf{m} \perp \mathbf{n}$ [39], yielding a sinusoidal modulation of the effective refractive index. This modulation is at the heart of the photonic performance of dried CNC suspensions, a second key component being the transition into a kinetically arrested gel state at a critical local CNC mass fraction w_k on the order of 10 wt.-% [12,40,41]. Evaporation of the remaining water then compresses the pitch p of the cholesteric helix to the range of visible light wavelengths, giving rise to the photonic crystal properties [42].

Throughout the Onsager biphasic regime the local volume fractions in the isotropic and nematic phases are ϕ_0 and ϕ_1, respectively, i.e., each phase is always at its stability limit. Even weak shear flow can then *induce* long-range orientational order in the fraction that is isotropic at rest into what is called a paranematic state [43–45], with the nanorods aligned along the shear as long as the shear persists [46]. Our findings below suggest that the ideal situation for breaking up nanorod bundles by sonication is when the paranematic state prevails throughout the sample volume, because the uniaxial long-range orientational order renders the ultrasound-induced shear maximally effective in disassembling agglomerates at the same time as it minimizes damaging impact between particles. When sonicating anisometric nanoparticle suspensions, one should thus consider working at W_s close to the stability limit of the isotropic phase, $W_s \approx W_0$. For most CNC suspensions $W_0 \ll w_k$, which is important because sonication-driven particle individualization works poorly on gelled suspensions (although sonication of gels can have very interesting global effects via the incurred vibrations [47]), and we find that gelation leaves strong impact in the form of end-to-end-agglomerated CNCs even after dilution.

To give evidence of the effects, we systematically vary W_s from fully isotropic, throughout the biphasic regime, into the fully liquid crystalline state, and even up to the point of complete gelation, and we film the suspensions between crossed polarizers during the sonication procedure. We then characterize the sonication-individualized CNCs by atomic force microscopy (AFM), and we study the LC phase behavior and equilibrium helix pitch of the corresponding suspensions, obtaining broad evidence of the impact of W_s on the resulting CNCs and their suspensions.

II. RESULTS

A. Characterization of the pristine CNC suspension

We work with commercial sulfuric acid-hydrolyzed CNC from CelluForce, sold as a water-based slurry with global CNC mass fraction $W = 6.4$ wt.%. Because sonication often changes the behavior of a CNC suspension in important ways, we add an asterisk in the following to parameters that apply specifically to this pristine CNC suspension. The information provided by the manufacturer and our macroscopic characterization results are provided in Appendix A. As described there, we estimate the biphasic regime to extend from $W_0^* \approx 2.2$ wt.% to $W_1^* \approx 5.1$ wt.%. The original slurry has the appearance of a weak gel that is easily broken by slight shear force, hence, this CNC type has an unusually low $w_k \leqslant 6.4$ wt.%. To establish a range of W in which macroscopic gelation can certainly be avoided, we dilute the pristine suspension stepwise and distribute the aliquots in vials that are first left standing for 3 weeks and then gently turned upside down. Up to $W = 4.5$ wt.% all suspensions immediately respond by flowing to the new bottom side of the vial, while for $W = 6$ wt.% the suspension stays at the new top, thus clearly being gelled at macroscopic scale. At $W = 4.75$–5.0 wt.% the suspension first stays at the new top but within a second it drops as one intact volume to the new bottom.

To correctly interpret these observations, we must take into account that the change in flow behavior occurs within the biphasic regime, which complicates the analysis. Moreover, we must adapt Onsager's theoretical and idealized framework to the practical situation of CNC suspensions. Appendix B contains a detailed account of the process, which yields the following key results. First, because the effective volume fraction per individual CNC decreases with increasing CNC content as a result of rising ionic strength, we work with CNC mass fraction W rather than volume fraction ϕ, defining

the biphasic regime by the practically accessible boundaries W_0 (corresponding to ϕ_0) and W_1 (corresponding to ϕ_1). Second, due to the separation within this regime into coexisting isotropic and nematic phases with different CNC contents, we must distinguish between *local* mass fractions w in a uniform subvolume of the overall suspension and the *global* mass fraction W of the entire suspension.

Third, we note that the dispersity in aspect ratio of CNCs leads to a much broader width ΔW of the biphasic regime than that predicted by Onsager for nondisperse nanorods, which can be understood as a consequence of the spontaneous fractionation induced by the phase separation [32,34,35]. Since it is the CNCs with the highest L_e/D_e that form the first tactoids after equilibration at W just above W_0, this threshold is rather low. In contrast, the last remaining isotropic phase at the end of the biphasic regime has low average L_e/D_e, yielding a high W_1. We find $\Delta W^* \approx 1.3 W_0^*$ for the pristine CNC suspension. Such broadening of the biphasic range is expected also for many other nanorods, e.g., carbon nanotubes, the suspensions of which also form nematic LC phases [48] and for which the same type of fractionation has been reported [33].

Another important consequence of the spontaneous fractionation is that the local w_0 and w_1 continuously increase with increasing W within the biphasic regime, thus deviating from the globally determined values W_0^* and W_1^* of the pristine suspension, which are valid only at the lower and upper boundary, respectively. To estimate the CNC content in the LC phase in the intermediate regime, we apply a simple heuristic interpolation as a function of the global mass fraction W, as motivated in Appendix B:

$$w_1 \approx W \cdot 1.36^{\frac{W_1 - W}{W_1 - W_0}} \tag{1}$$

Here W_0 and W_1 are the boundaries of the biphasic regime of a particular CNC suspension as determined on macroscopic samples. When applying Eq. (1) to the pristine CNC, $W_0 = W_0^*$ and $W_1 = W_1^*$, but for sonicated CNC the W_0 and W_1 values may differ strongly.

We are now ready to interpret the observed flow behavior, noting that at $W \approx 4.75$ wt.%, where the suspension is an easily broken gel, about 85% of the sample volume is liquid crystalline (see Fig. 7 in Appendix A). Because we are in the biphasic regime, the local w_1 must be greater than 4.75 wt.% but below the global nematic stability limit $W_1^* \approx 5.1$ wt.%. The transition in flow behavior suggests that $w_1 \geqslant w_k$, such that the liquid crystalline tactoids are gelled, and that at this borderline sample, we are at the threshold for percolation of tactoids. As a rough approximation sufficient for this paper, we may thus estimate $w_k \approx 5$ wt.% for the CelluForce CNC, probably somewhat lower. At $W = 6.0$ wt.% the entire sample is gelled, preventing all flow in response to gravity in these small vials. Larger volumes may still flow when the sample is inverted, because the greater gravitational force may break the weak gel.

B. Variations in long-range order, phase separation, and gelation before, during, and after sonication

Based on this information, we subject a set of aqueous suspensions to sonication under identical conditions, W_s varying from 1 wt.% to 6 wt.% in steps of 0.25 wt.%. All samples are prepared by diluting the original slurry with pure water and then gently homogenizing by manual shaking for about three minutes. We film the suspensions between crossed polarizers while they are being sonicated, see Supplemental Video 1 [49] and Fig. 1. To ensure that isotropic regions remain visible, we also place a birefringent foil that approximates the function of a first-order λ phase plate between the polarizers, giving all isotropic regions a dark violet color. The sonication lasts about one minute with a 50/50 cycle (0.5 s sonication, 0.5 s pause; this is a common choice to avoid local overheating), until a total sonication energy of 700 J has been delivered. With a sample volume of 40 mL, this corresponds to an energy density of 17.5 J/mL. The samples investigated by other methods are sonicated in the same way. We see strong impact of W_s on the response to sonication, and this response also varies in different ways during the minute that the procedure is ongoing.

To illustrate this efficiently, Fig. 1 shows snapshots from Supplemental Video 1 [49] before, during, and after the first cycle, after the mid cycle, during relaxation after the final cycle, and finally after 19 days of sedimentation along gravity. The video compiles the original videos from all samples next to each other to facilitate comparison. Several key observations provide critical information for understanding the impact of sonication at varying W_s.

(1) Prior to sonication, samples with $W_s \leqslant 1.75$ wt.% are fully isotropic at rest but light vibrations or gentle movement of the sonication tip induce birefringence (bright and/or colorful appearance) despite the fact that $W_s < W_0^*$. Even weak shear thus induces paranematic local order in these samples. For $2.0 \leqslant W_s \leqslant 2.25$ wt.%, the entire vial appears birefringent prior to sonication, with a static texture. With $W_0^* \approx 2.2$ wt.%, no birefringence in the absence of shear is expected below this threshold.

(2) During active sonication, all samples show birefringence together with strong scattering. In the pause following active sonication in the first cycle, samples with $W_s \leqslant 2.25$ wt.% show a characteristic schlieren texture with dark lines and colorful regions. This is typical of a paranematic state during its relaxation directly after shearing has stopped. For $1.5 \leqslant W_s \leqslant 3.25$ wt.%, the same holds for the first few seconds after the last cycle.

(3) For $W_s \geqslant 2.5$ wt.%, the texture is uniformly yellowish white prior to sonication due to strong light scattering from LC tactoids distributed throughout the sample volume. The cholesteric phase in tactoids exhibits helically modulated **n** along **m**, which is randomly oriented. The lack of macroscopic alignment of **n** and **m** is what causes the dominant scattering here. After the end of the final sonication, however, there is no scattering for $W_s \leqslant 3.25$ wt.%, indicating that the process effectively removes all helicoidally modulated LC phase even if it was present initially.

(4) Within 5 s after the end, vials with $W_s \leqslant 2.25$ wt.% are fully isotropic and those with $2.5 \leqslant W_s \leqslant 3.0$ wt.% are mainly isotropic, even if several of these samples showed paranematic or even stable birefringence before sonication. Upon gentle shear flow paranematic order can still be induced (Supplemental Video 2 [49]). At 19 days after sonication, the equilibrium cholesteric phase has sedimentated to the bottom in nongelled samples with $W_s \geqslant 2.5$ wt.%. The static

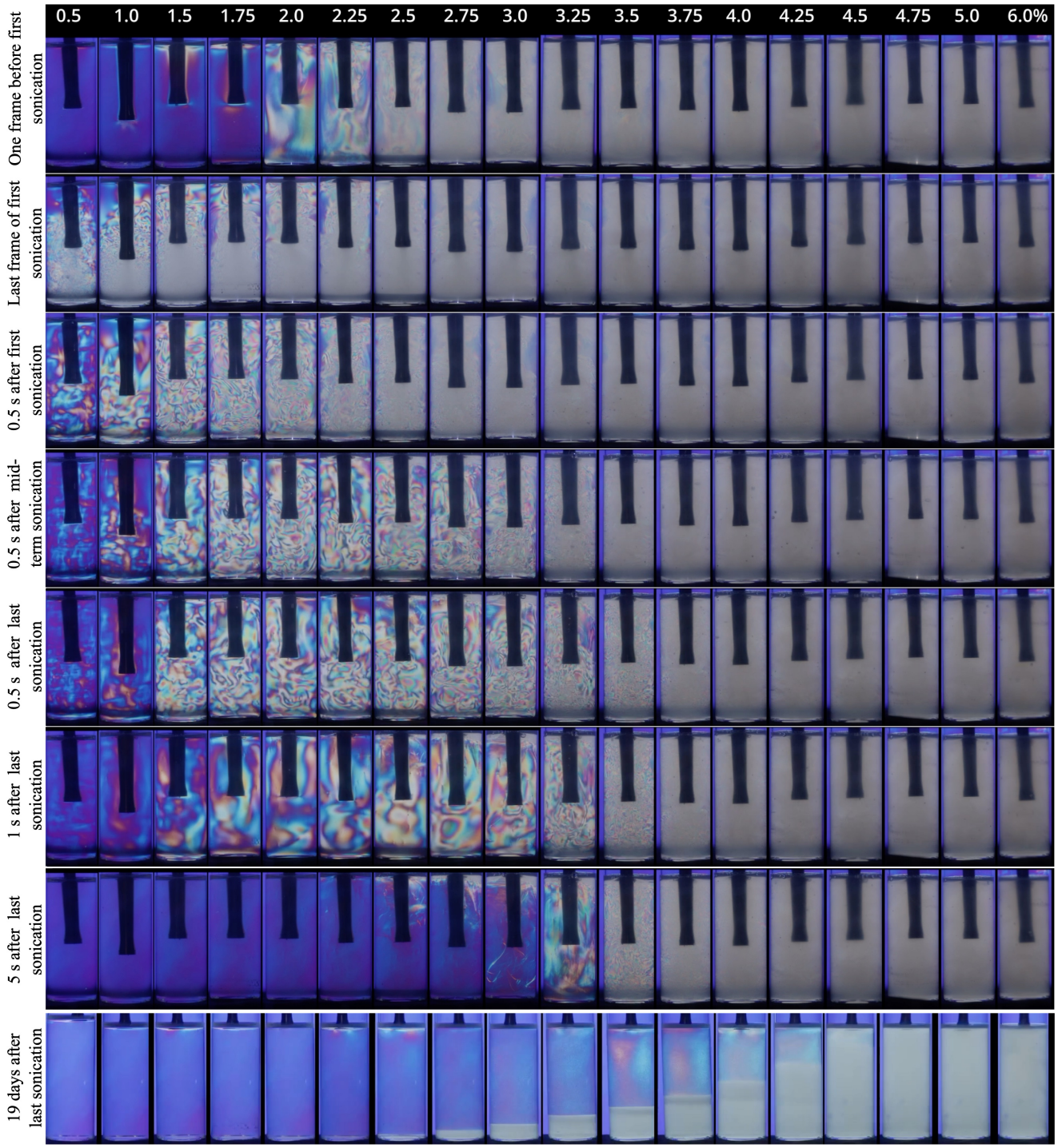


FIG. 1. CNC suspensions with W_s increasing from left to right (indicated along the top) at different stages of the sonication process (as indicated on the left; one frame is 1/25 s) as viewed between crossed polarizers with an inserted birefringent foil approximating the effect of a first-order λ phase plate. The black rod inserted from the top is the sonotrode tip; the top of each sample is the air interface and the bottom is the vial bottom. Each row is a still frame from Supplemental Video 1 [49]. The vial with $W_s = 0.5$ wt.% experienced one sonication cycle more than all others, hence the post-sonication images for this sample are taken 1 s after the corresponding images for the other samples.

vial-spanning colorful birefringent textures seen at $2.0 \leqslant W_s \leqslant 2.25$ wt.% prior to sonication are not recovered.

(5) For $W_s \geqslant 2.5$ wt.%, the regions that are not isotropic 5 s after the end of the final sonication retain a static texture after termination of sonication. These regions are seen close to the air surface and around the sonotrode, where the sonication is the weakest, while below the tip no birefringent regions are seen up to $W_s \leqslant 2.75$ wt.%. From $W_s = 3.25$ wt.%, the system looks identical below the tip and around it.

(6) For $W_s \geqslant 3.5$ wt.%, the system appears partially gelled from beginning to end, the texture being strongly scattering at all times during sonication and after.

We will identify the relevance of each of these observations, correlating with other data, in the Discussion.

We also measure the effective shear viscosities of non-gelled sonicated suspensions with varying W_s and compare with those of the pristine suspension at corresponding W, see Appendix C. At $W \approx W_0^*$, the pristine and sonicated data are similar regardless of flow rate, but as $W \to W_1^*$, the effective viscosity decreases after sonication, the difference being the greatest at low flow rates. Since the viscosity of LCs is orientation-dependent [50], the lowest value being for flow along **n**, this suggests that sonicated samples are more easily flow-aligned than pristine samples at the same W.

C. The impact of W_s on CNC individualization, phase diagram, and helix pitch

We now compare the impact of sonication on the geometrical features of individualized CNCs (as established using Atomic Force Microscopy, AFM), the CNC suspension phase diagrams, as well as the cholesteric helix pitch, as a function of W_s. Since we need samples over a wide W-range to establish the phase diagrams, we first upconcentrate the sonicated samples to W in the range 4.9–7.9 wt.% (details in Appendix D) by evaporating water during constant stirring. The resulting samples are strongly vortex-mixed for several minutes immediately prior to distribution of aliquots into vials for dilution to obtain equal volumes with $W = 1.0$–4.5 wt.% in steps of 0.5 wt.%. The aliquots for AFM investigation are taken from subsamples diluted to $W = 2.0$ wt.%, each confirmed to be fully isotropic in the absence of shear by observation between crossed polarizers. This means that there is no phase separation within the volume, ensuring that each aliquot investigated by AFM is representative of the entire sample. Each AFM aliquot is again strongly diluted prior to the experiment to achieve a suitable density of CNCs on the chip.

When assessing the AFM data, we first analyze the phase images to exclude all CNCs that remain in bundles, since we are interested in the features of individualized CNCs and the damage on them imposed by the sonication. We have explored several tools in two different image analysis software to try to automate this distinction but so far did not get satisfactory results. The distinction is therefore done manually by studying both the height and phase images from the AFM data (see Appendix E), which introduces a subjective component, hence the data must be interpreted with caution. Because AFM gives highly accurate data for height (Δz) over the substrate but has difficulties measuring small in-plane widths Δx or Δy accurately (explanation in Appendix E), we use Δz as an estimate for the CNC lateral dimension. Given that the CNC is likely to rest on the substrate with maximum cross-section in contact, the height signal should correspond mainly to the CNC thickness T. One should note, however, that the Δz value provided by the software corresponds to the maximum height along a measuring line, hence it is an upper limit of T. In many cases, it may overestimate the actual CNC thickness, because a local twist in the rod will bring B into the height direction, and a kink may lift a local section of the CNC from the substrate. For this reason, very large $\overline{T}$ values may not be representative.

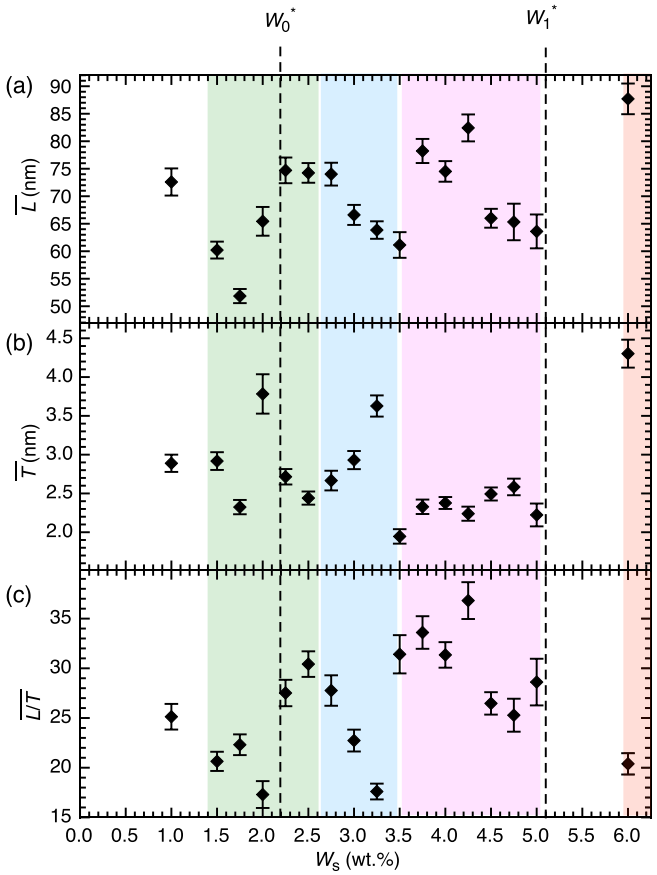


FIG. 2. Impact of W_s on individualized CNC average length $\overline{L}$ (a), average thickness $\overline{T}$ (b) and average aspect ratio $\overline{L/T}$ (c). Four regimes with qualitatively different behavior are highlighted with different background colors. Each sample has a volume of 40 mL during sonication at an amplitude of 40% to a total sonication energy of 700 J. Error bars represent the standard error of the sample mean, i.e., they represent the confidence in establishing each mean value, not the dispersity of the suspension. An estimate of the latter is given by the standard deviations, which are obtained by fitting a log-normal distribution to binned L and T distributions from around $n \approx 200$ individual measurements (see Appendix E). Note that all CNCs that are deemed to be part of a bundle, following manual assessment, are excluded.

The results are presented in Fig. 2, where we have indicated the boundaries $W_0^* = 2.2$ wt.% and $W_1^* \approx 5.1$ wt.% of the biphasic regime of the pristine CNC. We may roughly distinguish four regimes of qualitatively different behavior as W_s increases, indicated with different background colors in Fig. 2. First, for $1.4 < W_s < 2.6$ wt.% (green background), the average aspect ratio $\overline{L/T}$ shows a trend of consistent increase by about 50% from ∼20 to ∼30, except for the outlier at $W_s = 2.0$ wt.%. The reason for the low apparent aspect ratio is a $\overline{T}$ value that is much greater than the surrounding data points and which also has a particularly large error. As mentioned above, large T values may be due to unrepresentative kinks or twists in the CNCs, hence the outlier is likely an artifact.

In the second regime (blue), $2.6 < W_s < 3.5$ wt.%, we instead see a consistent decrease of $\overline{L/T}$ to below 20. This is mimicked by an equally consistent decrease in $\overline{L}$ and an

increase in $\overline{T}$. In the third regime (pink), $3.5 < W_s \leqslant 5.0$ wt.%, $\overline{L/T} \approx 30$ but the values are quite scattered, mainly due to strong scattering in $\overline{L}$ while the $\overline{T}$ values are consistently low. The fourth regime (red), finally, is represented by the single sample at $W_s = 6.0\%$, which is fully gelled from the start. Here $\overline{L/T}$ drops to about 20 while both $\overline{T}$ and $\overline{L}$ have exceptionally high values.

Because the sonication amplitude is known to have a strong impact on the results, we carry out our investigations at three different amplitudes, at 40% in Fig. 2, identical to the sonication in Fig. 1, but also at 30% and 50% amplitude, respectively, see Fig. 15 in Appendix E. In general, we recognize the trends from the 40% series within the green, blue, and pink regimes, with $\overline{L/T}$ increasing as W_s passes from isotropic to W_0^* and slightly above (green), and then decreasing as W_s approaches the middle of the biphasic regime (blue). As expected, the amplitude influences $\overline{L}$ which generally decreases with increasing amplitude. The $\overline{T}$ values are often much greater for 30% amplitude than the corresponding values for 40–50% amplitude, suggesting that 30% amplitude is too weak for efficient debundling. In contrast, from 40% to 50%, no clear decrease can be seen in $\overline{T}$. Given that $\overline{L}$ is reduced when using 50%, this amplitude appears unnecessarily high. Such high-power sonication may be of interest as an initial treatment in case practical circumstances require the sonication to be applied to a gelled suspension, since vibrating a colloidal gel via high-power sonication can assist to fluidize it [47]; once it starts flowing the sonication amplitude can be reduced to minimize particle damage.

To assess the impact of W_s on the phase diagram, we let the vials with different W prepared from each sonicated sample stand for six weeks of equilibration. We then photograph all vials between crossed polarizers to measure the volume fraction Φ_{LC} of cholesteric phase as a function of W, once more also after one year (Appendix D). Across the biphasic window, Φ_{LC} increases monotonically with W, slightly sublinearly as a result of the particle dispersity. For simplicity, we model the behavior with the linear approximation:

$$\Phi_{\mathrm{LC}} \approx \frac{W - W_0}{W_1 - W_0}. \tag{2}$$

This works quite well for our CNC suspensions, with the caveat that data points falling on a superlinear curve should not be included when fitting Eq. (2) to experimental data, since such points are artifacts due to gelation (see further discussion below).

In Fig. 3(a), we plot the obtained phase diagrams on the form Φ_{LC} versus W for three selected series, sonicated with 40% amplitude at $W_s = 1.5$, 2.25, and 4.0 wt.%, respectively, as well as for the pristine CNC. Figure 3(b) shows the bulk isotropic and cholesteric stability limits W_0 and W_1 for the sonicated series as a function of W_s. The data are obtained by fitting Eq. (2) to the experimentally observed $\Phi_{\mathrm{LC}}(W)$. For reference, Fig. 3(d) reproduces the $\overline{L}/\overline{T}$ data from Fig. 2, and we use the same color coding as in that figure to highlight the three regimes without macroscopic gelation. We remind that the latter data were obtained following a rejection of bundles based on manual assessment, hence they may not be fully representative of the macroscopic behavior of the CNC suspensions. We find that W_0 and W_1 after sonication,

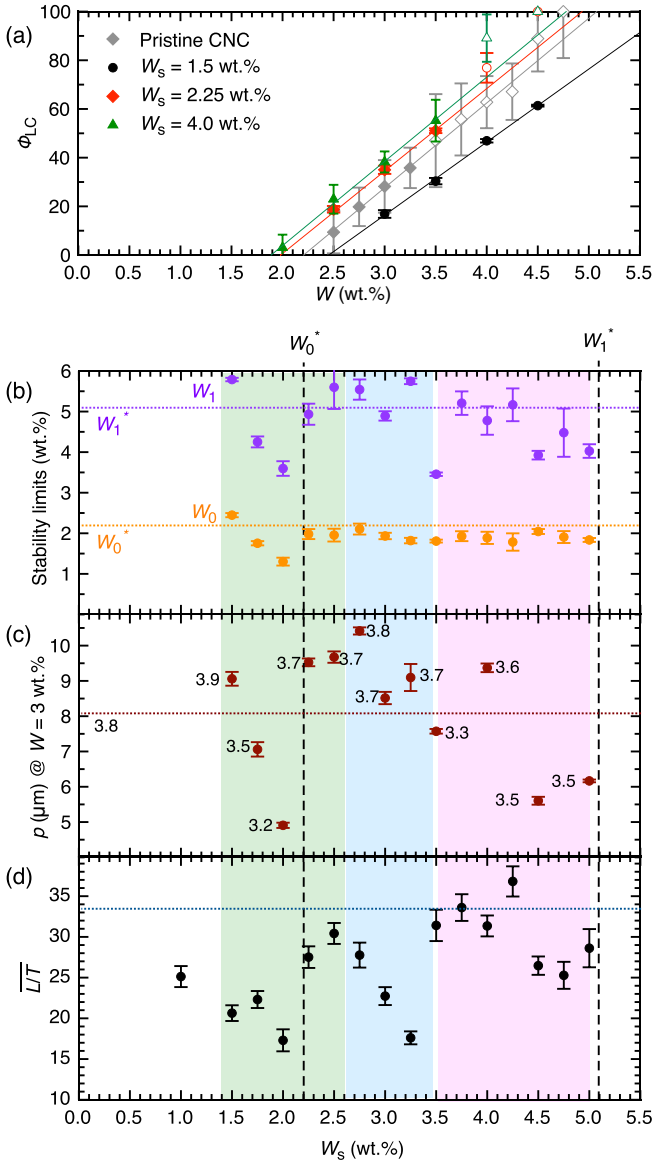


FIG. 3. Impact of W_s on phase behavior, helix pitch, and individualized CNC aspect ratio. (a) Volume fraction Φ_{LC} of LC phase as a function of global CNC mass fraction W for three samples sonicated at different W_s (indicated in the legend) as well as for the unsonicated pristine suspension. Filled symbols show data points used when fitting Eq. (2) to the data, whereas unfilled symbols show data points excluded during fitting. (b) Stability limits W_0 and W_1 of the sonicated CNC suspensions as a function of W_s. The stability limits of the pristine suspension, W_0^* and W_1^*, are indicated with horizontal dotted lines. (c) Helix pitch p at $W = 3$ wt.% as a function of W_s. Next to each data point is given the estimated value of w_1 since this is the local CNC mass fraction in the cholesteric phase where the helix pitch is measured. The dotted horizontal line shows p of the pristine suspension at $W = 3$ wt.%, its estimated w_1 value written below the line on the left. (d) Average CNC aspect ratio $\overline{L/T}$, reproduced from Fig. 2, as a function of W_s. The horizontal dotted line shows $\overline{L/T}$ of the pristine CNC suspension, as established from the data in Fig. 12.

both decrease as $W_s \to W_0^*$ from $W_s = 1.5$ wt.%: for both stability limits, a distinct minimum is seen at $W_s = 2.0$ wt.%. For $W_s = 2.25$ % and higher, W_0 is nearly constant around

2 wt.%, thus close to but somewhat lower than W_0^* of the pristine suspension. As for W_1, its vicinity to w_k renders it difficult to establish with accuracy, and the data fluctuate strongly. As explained below, the W_1 data must be interpreted with care.

Concerning the helix pitch p (Appendix F contains texture images from which the values were measured), we first note that, since p depends on the local CNC mass fraction w_1 of the cholesteric phase as well as on the effective helical twisting power (HTP) of the CNCs in that phase [39], which has been proposed to scale with the CNC length [35] or with the fraction of CNC bundles [51,52], it is not obvious under what conditions to measure the pitch for each suspension. For consistency, we choose a constant value of $W = 3$ wt.%, in the biphasic region and close enough to W_0 to avoid gelation of the LC domains. We use Eq. (1) with the W_0 and W_1 data plotted in Fig. 3(b) to estimate w_1 at $W = 3$ wt.% for each value of W_s, as indicated next to each data point in Fig. 3(c). While these values are only estimates, they are more representative of the actual CNC content for which p is measured than W.

In Fig. 3(c), we distinguish two regimes for the p versus W_s behavior. Similar to the stability limits, we first see a strong monotonic pitch decrease from $p \approx 9.5$ to ≈ 6 μm as $W_s \to W_0^*$ from $W_s = 1.5$ wt.%. We note that, due to the decreasing W_0 and W_1 in the same sequence, the local CNC content consistently decreases from $w_1 \approx 3.9$ wt.% to $w_1 \approx 3.2$ wt.%. In other words, both p *and* w_1 decrease, a situation that can only be explained by an increasing HTP of the CNCs present in the cholesteric phase as W_s increases from 1.5 to 2.0 wt.%.

Also for sonication in the biphasic regime, we see an overall trend of decreasing p on increasing W_s, but the data are rather scattered. At $W_s = 2.25$ wt.% p gets much longer than at $W_s = 2.0$ wt.%, fluctuating around a value of about 9.5 μm as W_s increases to 3.25 wt.%. With W_s approaching W_1^* the pitch shortens, but it never reaches the low value seen with $W_s = 2.0$ wt.%. The local CNC mass fraction is fairly constant across the biphasic regime, most series having w_1 around 3.6–3.8 wt.%, somewhat lower for $W_s = 4.5$ and 5.0 wt.%. In other words, also in this regime we find the unexpected correlation of large pitch with high CNC mass fraction, and vice versa, suggesting that HTP of the CNCs in the cholesteric phase changes across the biphasic regime as well, again increasing on increasing W_s.

III. DISCUSSION

A. How W_s affects the efficiency of debundling

What is the reason for the strong impact of W_s on the sonication process and which conditions are the most beneficial in terms of maximizing CNC individualization while minimizing damage? To answer these questions, we need to consider what happens in a nanorod suspension during sonication. In the pristine sample, we may roughly distinguish between three kinds of bundle: primarily side-to-side [Fig. 4(a)], primarily end-to-end [Fig. 4(b)], and crossed nanorods [Fig. 4(c)] [27,53]. The second category was found by Honorato-Rios *et al.* to be particularly prevalent if $w \to w_k$ [34], most likely a result of the different surface chemistry at CNC sides and ends [54], which may give lower surface charge and thus local

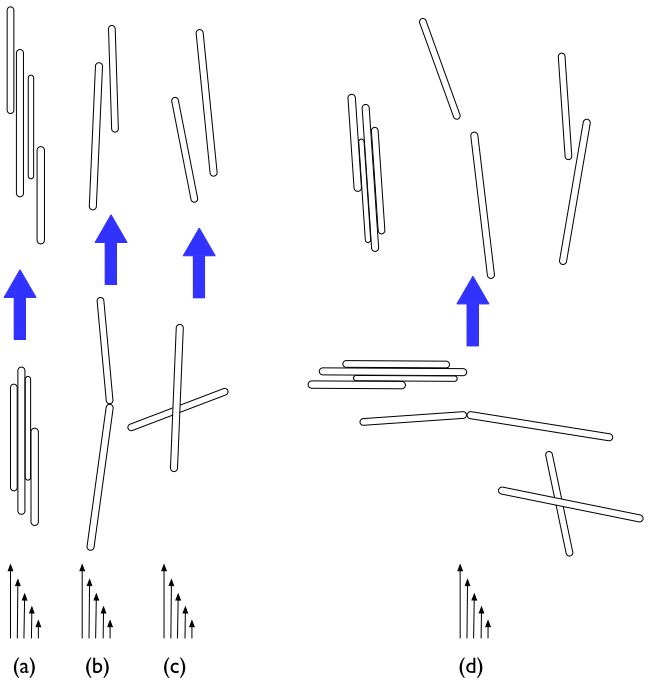


FIG. 4. Highly idealized drawings of the impact of sonication-induced shear flow on different types of bundles. The bundles are oriented with their longest axis perpendicular [(a)–(c)] and along (d) the shear gradient, horizontal in the drawing. The flow profile is indicated at the bottom, acting on the original bundles sketched above the flow profile. The top drawings illustrate the result of the shear flow on each type of bundle, promoting separation when the shear gradient is perpendicular to the average bundle axis.

minima in colloidal stability at the CNC ends [39]. Theoretical analysis also showed that the combination of nematic order and high connectivity, as expected when $w \to w_k$, promotes linear chain formation along **n** [55].

The purpose of sonication is to break up all bundles as efficiently and easily as possible, with a minimum negative impact in the form of damaged nanorods. Sonication-induced debundling happens because of the very strong local shear and extensional flows arising as a result of the acoustic field oscillating gas bubbles, which eventually collapse (cavitation) [1,2]. If the gas is present from the start, e.g., as air bubbles, we speak of extrinsic cavitation, while intrinsic cavitation can happen at sonication intensities strong enough to locally evaporate the solvent into its vapor phase. In the direct vicinity of an oscillating bubble, the liquid flow velocity is oriented radially and scales with the square of the distance from the bubble center [24]. A bundle or CNC that is perfectly aligned radially and that is so slender that it does not experience any local variation of flow direction experiences only the extensional flow caused by the radial flow velocity scaling. This is very efficient in separating end-to-end-connected CNCs, and it can even lead to scission of individual CNCs, albeit only down to a limiting length. Following the model of Huang *et al.* [24], we estimate the limiting length of CNCs to be on the order of 100 nm, which is similar to the typical length of our individual CNCs, i.e., we do not expect strong scission of CNCs due to extensional flow in our study. Such scission must

have happened during sonication in the production process, explaining why the CNCs are already close to their limiting length.

Here we focus mainly on the shear flow that results from the radial variation of flow direction, considering the flow along the central radius as the vertical direction. Also further away from any specific bubble, where the flow pattern can be quite complex, the particles will experience strong shear flow. Figure 4 shows highly simplified schematics of the impact of shear flow on the three types of bundles, considering that they are oriented perpendicular [(a)–(c)] or along the shear gradient (d). The former situation applied to a bundle of side-to-side-agglomerated nanorods [Fig. 4(a)] should be efficient in tearing the individual nanorods away from each other without further damage, since each rod experiences a different flow rate and since the bundle is kept together mainly by noncovalent bonds (hydrogen bonds and van der Waals interactions for CNCs). As a result, the individualized nanorods translate along the flow. Also end-to-end-agglomerated rods may be separated in this favorable way if they are originally aligned perpendicular to the shear gradient on average [Fig. 4(b)], since a slight misorientation from one rod to the next will make one translate faster than the other, tearing them apart at their attachment location and then translating the individual rods along the flow.

If either type of bundle is oriented along the shear gradient, however, the entire bundle will rather be rotated by the shear, which here is not favorable for breaking up agglomerates. The nanorods will instead experience internal stress. An end-to-end-agglomerated bundle is likely to be broken up also in this orientation, given the small contact area between the rods making up the bundle (Fig. 4(d), middle). When sonication is done at W_s so low that the suspension is isotropic most of the time, any orientation with respect to the shear flow is equally likely, hence there are as many side-to-side bundles that mainly rotate as bundles that are separated into individual rods. A crossed-rod bundle is always rotated since it cannot be oriented perpendicular to the shear gradient, but also here the contact area between rods is small, hence break-up is likely regardless of orientation [Figs. 4(c) and 4(d), right].

The rapid and repeated translative motion during sonication of individualized nanorods and bundles means that the process also raises the likelihood and frequency of violent particle-particle impact during sonication, which is known to be strong enough to break covalent bonds, in particular when internal stresses already exist. Such collisions provide another mechanism for scission of anisometric nanoparticles, effectively reducing the aspect ratio. An isotropic suspension maximizes the likelihood of such scission-inducing particle-to-particle or bundle-to-bundle impact, since the lack of long-range orientational order gives a short mean free translation path. These considerations may explain why $\overline{L}$ is low, reaching values well below the saturation length from extensional flow [24], after sonication at W_s below W_0^*, see Fig. 2.

When the suspension has $W_s \approx W_0^*$, however, we are at the limit of long-range orientational order developing, and even slight shear pushes the system over the boundary to where the rods align in the paranematic state. This means that the sonication-induced shear flow does not only act on individual bundles, but it acts on the entire *phase*, aligning *all* bundles along the shear flow, as is optimum for efficient individualization with minimum particle damage. Moreover, when all individual rods and bundles translate along the same direction, which is along their long axis orientation, the average mean free path is maximized and the likelihood of particle-particle impact is minimized. In fact, this gain in translational entropy at the cost of rotational entropy is the very reason why an LC phase forms in suspensions of rod-shaped particles [37]. To summarize, $W_s \approx W_0^*$ should ensure maximally efficient debundling while minimizing the risk of collisions or unfavorable internal stress.

Such improved individualization without breaking, thus increasing the effective particle aspect ratio, also correlates well with the reduction in W_0 and W_1 as well as in p (corresponding to increasing HTP of the CNCs present in the cholesteric phase) as W_s approaches W_0^* from lower values. For the stability limits, this follows directly from the Onsager theory, while the HTP increase is consistent with a previous observation that higher aspect ratio CNCs yield greater HTP [35]. As mentioned above, the very low outlier value for $\overline{L/T}$ at $W_s = 2.0$ wt.% is likely an artifact due to our $\overline{T}$ values being upper estimates; if this value were correct, Onsager theory would predict a particularly high W_0^* value for this sample, in contrast to what is seen in Fig. 3(b).

As W_s increases beyond W_0^*, sonication starts while the tactoid fraction of the sample is spontaneously long-range ordered, now with the helical modulation of a cholesteric phase imposed. As shown previously [35], the highest aspect ratio CNCs (individual and/or agglomerated) predominantly localize within the tactoids, leaving the isotropic regions depleted from such particles. Emersic *et al*. recently demonstrated that a cholesteric phase responds to shear by orienting the helix axis **m** along the shear gradient [56]. In this way, the director **n** is never perpendicular to the shear gradient, and we should thus have quite efficient CNC individualization also within the tactoids. However, **n** is along the shear direction only twice per helix pitch, and the mean free path is low due to the small size of tactoids. Compared to the paranematic state, we may thus expect less debundling and an increasing degree of rupture of individualized CNCs as Φ_{LC} increases during sonication, at least until the shear flow has been active long enough to unwind the helix, thereby allowing fusion of tactoids and their paranematic surrounding. The time required to reach this state should increase with increasing W_s, and this is indeed what we can see by studying the textures during the rest phase of sonication in Supplemental Video 1 [49]. This would explain the decreasing aspect ratio in the second (blue) regime in Figs. 2 and 3. For nonchiral nanorods that develop a nematic phase without helical modulation, sonication at W_s slightly greater than W_0^* may be even better, as the spontaneous long-range orientational order should be beneficial, in contrast to the cholesteric case.

A complication for $W_s > 3$ wt.% is that the local CNC mass fraction in the tactoids, w_1, approaches the kinetic arrest threshold w_k. The scenario just mentioned, when equilibrium tactoids are eventually dissolved after shear-induced helix unwinding and replaced by a uniform paranematic state during sonication, is much less likely to happen when the viscosity in tactoids diverges as their contained phase approaches gelation.

Rather than dissolving such tactoids, sonication may break them up into smaller gelled 'particles' which retain their local high mass fraction of predominantly high-aspect-ratio CNCs and CNC bundles, with their helically modulated long-range order intact. This explains why the suspensions at high W_s remain scattering throughout the entire sonication procedure in Fig. 1 and Supplemental Video 1 [49].

The $W_s = 3.5$ wt.% deserves special attention, as it is at two borders: it separates the second and third regimes in Figs. 2 and 3, and in Fig. 1, it is between the low-W_s regime where the vial after completed sonication shows schlieren rather than scattering, indicating a dissolution of tactoids and unwinding of the helix by sonication, and the high-W_s gelled regime where the sample hardly changes during sonication. The $W_s = 3.5$ wt.% sample apparently has the lowest W that yields $w_1 \geqslant w_k$, i.e., its tactoids are fully gelled, whereas those in biphasic samples with $W_s < 3.5$ wt.% may get more viscous with increasing W_s, but they still respond to the shear flow. At the same time, the $W_s = 3.5$ wt.% sample contains a large volume fraction of isotropic phase, which is not gelled and which thus develops paranematic order with many individualized CNCs translating along the shear flow. However, they will frequently collide with the ubiquitous gelled tactoids present in this sample. The low $\overline{L}$ in this sample would thus result from the longest CNCs being trapped in gelled tactoids, where they remain in bundles and are thus excluded in Fig. 2, and by the remaining CNCs being shorter from the start, and in addition, suffering more damaging collisions with gelled tactoids.

The sudden increase in W_0 and W_1 and in p immediately as W_s enters the biphasic regime is interesting and unexpected. The fact that W_0 is now back to almost what it was in the pristine suspension suggests that already a small amount of spontaneously formed tactoids leads to reduced efficiency in debundling compared to when the entire volume is in a paranematic state. Indeed, the fact that all vials in this regime scatter light even at the end of the pause phase of the first sonication cycle shows that sonication does not immediately dissolve the spontaneously formed helicoidal order; this happens only towards the end of the entire sonication process.

For $W_s > 3.5$ wt.%, we see little variation in CNC geometry as well as in W_0 and W_1. This is understandable as we saw in Fig. 1 that these samples are largely gelled throughout the volume during the entire sonication process, without any sign of uniform order even at the end. The debundling is thus relatively inefficient but there is also little translation, with reduced collisions as result, yielding nonoptimum individualization but also moderate particle damage. What is less obvious to explain is why the helix appears to become shorter, and HTP greater, with increasing W_s in this regime. We conjecture that it is due to the phase separation-induced spontaneous fractionation of high-aspect-ratio bundles into the original tactoids, which are never broken up due to the locally gelled state. Thus these suspensions contain a high fraction of long CNC bundles, acting as 'chiral dopants' as suggested by Parton *et al.* [51], but they also have exceptionally high aspect ratios as a result of the spontaneous LC fractionation. This might be a way of unifying the reports of Parton *et al.* and Honorato-Rios and Lagerwall [35] into one framework.

B. Kinetic arrest has consequences that remain even after dilution

A striking observation from the sonication analysis is that, prior to sonication, some suspensions show birefringence in the absence of flow, despite having $W_s < W_0^*$, yet all suspensions with $W_s \leqslant 3.0$ wt.% end up predominantly isotropic within 5 s after sonication is terminated. These suspensions are also less prone to developing shear-induced paranematic order than they were before sonication, as shown in Supplemental Video 2 [49]. At first sight, sonication would thus appear to counteract LC formation in this regime, a highly counterintuitive conclusion considering that we clearly see how the shear flow of sonication promotes paranematic ordering and that the AFM analysis suggests that long-range orientational order promotes debundling into high aspect ratio individual CNCs.

To give a better explanation, we hypothesize that the suspensions contain end-to-end-agglomerated CNC chains [as in Fig. 4(b)] prior to sonication as a result of nematic order coupled with localized loss of colloidal stability [39] in the original slurry, which has $W > w_k \approx W_1^*$. Note that the diluted suspensions were only gently homogenized by manual shaking prior to sonication, hence there was little mechanical action to disrupt chains. These chains can have a very high effective aspect ratio, inducing nematic order at $W < W_0^*$, since W_0^* is determined for suspensions without chains (when establishing the pristine phase diagram, all samples were vortexed strongly after dilution, which we show below gives enough shear flow to break up the chains if $W \approx W_0^*$).

The increase in effective aspect ratio resulting from the connection of CNCs into long chains also greatly reduces the percolation threshold [57] and thus promotes gelation via rigidity percolation, i.e., the chains form a volume spanning network that triggers gelation at unusually low CNC content. This effect is enhanced by the peculiar physics of percolation in combination with nematic order, which is dominated by connectivity and promotes chain formation along **n** [55], hence reduced colloidal stability and long-range orientational ordering act synergistically to promote percolation and even reinforce the chain formation. A further contribution is provided by the high length dispersity of CNCs, since the presence of short rods promote percolation within a nematic phase [58]. The static nature of the initial birefringent textures, hardly responding even to induced flow, may thus be explained as a consequence of rigidity percolation triggered by CNC chain formation. This effect is the most striking in the $W_s = 2.0$ wt.% sample in Fig. 1, which also happens to show the strong outlier in $\overline{T}$ in Fig. 2. Its excessively high value may thus be related to the presence of CNCs connected into macrochains in this nonequilibrium gelled component of the sample, since the chains are remnants of the original macroscopic gel at $W_s > w_k$.

To test this hypothesis, we conduct one additional experiment as follows: suspensions sonicated at $W_s = 1.75$ wt.%, 2.0 wt.% and 2.25 wt.%, respectively, which are all fully isotropic after sonication (see Fig. 1), are upconcentrated to $W = 4.9$ wt.%—thus $W \approx w_k$—and $W = 5.6$ wt.%—clearly above w_k—respectively. We then dilute all suspensions back to their original concentration, homogenizing first by manual

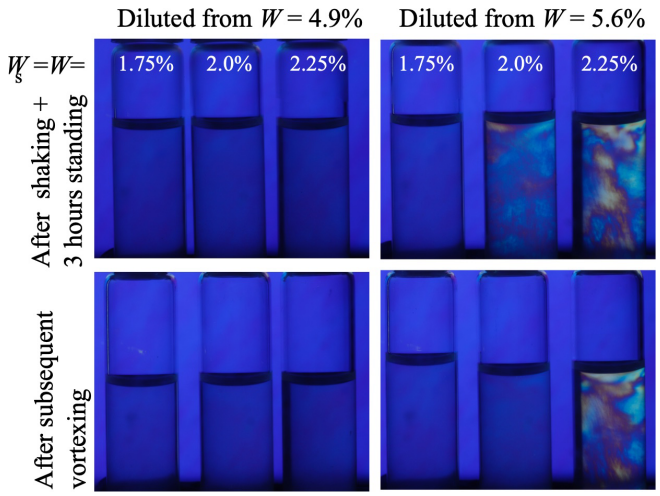


FIG. 5. Three CNC suspensions sonicated at $W_s = 1.75$, 2.0 and 2.25 wt.%, respectively, are split into two series which are upconcentrated to $W = 4.9$ and 5.6 wt.%, respectively, and then rediluted back to the original concentrations and imaged between crossed polarizers with a birefringent foil yielding a violet background. The samples are distributed into smaller vials, shaken manually and left standing (top row). After three hours, they are vortex-mixed (bottom row). While samples in the $W = 4.9$ wt.% series are fully isotropic after shaking and standing, the $W = 2.25$ wt.% sample diluted from $W = 5.6$ wt.% retains birefringence even after vortex mixing.

shaking and, three hours later, additionally by vortexing. We investigate them for presence or absence of birefringence after the shaking, after the subsequent standing, and after the vortexing, as shown in Supplemental Video 3 [49] and Fig. 5. We see a striking difference between the two series: while all suspensions that were upconcentrated to $W = 4.9$ wt.% are almost fully isotropic immediately after the homogenization by shaking, with only weak signs of birefringence and tactoids being detectable primarily in the $W = 2.25$ wt.% sample, the suspensions with $W = 2.0$ wt.% and $W = 2.25$ wt.% that were diluted from the suspension upconcentrated to $W = 5.6$ wt.% show striking schlieren patterns through the entire vial volume, just like the corresponding samples in the sonication experiment prior to sonication (Fig. 1).

In Supplemental Video 3 [49], we show the dynamic response of all six diluted suspensions at this stage when a metal rod is slowly inserted into the suspension and then gently retracted. All suspensions that are primarily isotropic at rest are highly dynamic, showing strong paranematic ordering during shear, which disappears quickly afterwards. In contrast, although the two vials with static birefringence also respond during motion, the texture is arrested almost immediately after. Interestingly, the arrest happens faster at $W_s = 2.0$ % (static after less than 1 s) than at $W_s = 2.25$ % (slow relaxation over a few seconds), which may be because the latter is above the threshold for liquid crystal formation. This sample is phase separated, with the highest aspect ratio CNCs withdrawn into equilibrium liquid crystal tactoids, which flow while being birefringent.

After standing for three hours, the samples prepared by diluting the suspensions upconcentrated to $W = 4.9$ wt.% have lost all signs of birefringence and the tactoids have been fully dissolved, see the upper left photo in Fig. 5. For the samples prepared from $W = 5.6$ wt.%, this holds only for the $W = 1.75$ wt.% sample, whereas the $W = 2.0$ and 2.25 wt.% samples remain largely unchanged, with large-scale birefringent textures, see the upper right photo. If the vials are now vortex-mixed, nothing changes for the four vials that had turned fully isotropic by standing, but the $W = 2.0$ wt.% sample prepared from $W = 5.6$ wt.% now also loses its birefringence. However, the $W = 2.25$ wt.% sample from this series remains birefringent, showing that even vortex mixing will not disrupt all end-to-end-connected CNCs if the concentration is high enough.

The important lesson from this experiment, which corroborates very recent observations by Ballu *et al.* [59], is that one should avoid concentrating CNC suspensions to $W > w_k$, if possible, to avoid unexpected effects. Clearly, once the sample is fully gelled, CNCs are strongly linked into chains that may persist even after dilution, yielding suspensions with unpredictable behavior that are not representative of suspensions with individualized nanorods. Sonication is effective at breaking up the chains, explaining why no sonicated samples that are kept at $W = W_s$ show birefringence at unexpectedly low W values. Also, the $W = 4.9$ wt.% sample should be gelled within the tactoids prior to dilution, given that $w_1 > W$ in the biphasic regime, which is why we still see some weak birefringence and even some very small tactoids after dilution in Supplemental Video 3 [49]. In contrast to the samples concentrated to $W = 5.6$ wt.%, however, dilution is apparently sufficient here to dissolve CNC chains and nonequilibrium tactoids if given enough time, as we see fully uniform textures with no trace of remaining birefringence after three hours of standing after dilution, as shown at the top left of Fig. 5.

These observations have an impact on our own studies of the phase diagrams: since the establishment of the full phase diagram requires concentration to W_1, and since for the CNC provided by CelluForce $w_k < W_1$ (in most cases even after sonication), we cannot avoid upconcentrating to $W \approx w_k$ if we wish to establish the phase diagrams. We cannot sonicate each sample a second time as this could have a further impact on the CNCs, hence our phase diagrams may be affected by CNC chains, especially at higher values of W. For this reason, we include in Fig. 3(a) only the three post-sonication phase diagrams where the upconcentration was limited to $W = 4.9$ wt.%, and we should consider the W_1 values in Fig. 3(b) as rather unreliable. We do not see evidence of the chain formation in our AFM images, which is to be expected since all vials selected for AFM investigation were strongly vortexed and confirmed to be fully isotropic. Moreover, the strong final dilution with subsequent vortexing done prior to AFM investigation should disrupt any minute presence of CNC chains that might not have been detected in the crossed polarizer test.

IV. CONCLUSIONS AND OUTLOOK

We have demonstrated that the particle mass fraction W_s at which nanoparticle suspensions are sonicated has a strong impact if the suspensions undergo a phase transition from isotropic to (chiral) nematic upon increasing W_s. An ideal situation for efficient individualization with minimum particle damage is achieved around the stability limit of the isotropic

phase of the pristine suspension, $W_s \approx W_0^*$. The sonication-driven shear flow then induces a transition to a macroscopically aligned paranematic state throughout the suspension volume, in which particle bundles are optimally aligned for individualization while the mean free path without damaging collision is maximized. Also the macroscopic physical parameters such as cholesteric helix pitch and stability limits of the isotropic and liquid crystalline phases are affected by W_s.

For W_s within the biphasic window, the situation in highly disperse nanorod suspensions such as CNCs is complicated by the spontaneous fractionation of the longest CNC bundles into liquid crystalline domains with a higher particle mass fraction than in the isotropic surroundings, as well as by the tendency for the suspension to gel when the local particle fraction gets high enough. This leads to the coexistence of phases which are different in physical state, particle concentration as well as particle dimensions. If the threshold for kinetic arrest is lower than the nematic stability limit, $w_k < W_1$, as for the CNCs used for this study, we additionally must consider effects of nonequilibrium gelation at least within parts of the suspension. This renders accurate analysis of macroscopic behavior difficult, especially since the effects of gelation may persist even after dilution from $W \geqslant w_k$, most likely in the form of chains of end-to-end-agglomerated CNCs. We are planning a follow-up study with a different CNC type with greater w_k, such that the impact of gelation and LC formation during sonication can be separately studied. It may also be beneficial to initially fractionate the unsonicated CNC suspension and study the impact on sonication only on the fraction with the highest aspect ratio CNCs and CNC bundles, since then the stability limit of the nematic phase can be kept well below the threshold for gelation, $W_1^* \ll w_k$ [34].

Because both nanoscopic features and macroscopic behavior of our CNC suspensions benefit from $W_s \approx W_0$, and because this observation should apply to any anisometric nanoparticle type capable of developing long-range orientational order in suspensions—possibly with subtle variations for chiral and nonchiral particles—any work involving sonication of such nanoparticles should be based on a strategic choice of W_s. Moreover, the finding that temporary gelation of a CNC suspension can strongly affect its macroscopic behavior even after it has been diluted may apply also to other anisometric nanoparticles if they are crystalline in nature, since they can then be expected to also have different surface chemistries at their smallest and largest surfaces. Taking these conclusions into account will benefit academic research, giving more reproducible behavior, as well as applications, since nanoparticles like CNCs, carbon nanotubes, graphene flakes, and many others can then be processed with a high degree of control to develop their optimum performance.

V. MATERIALS AND METHODS

A. Cellulose nanocrystals and establishment of phase diagrams

We purchased commercial sulfuric acid-hydrolyzed CNC from CelluForce, Montreal, Canada, delivered as aqueous suspension with $W = 6.4$ wt.%. Information on key parameters provided by the supplier is presented in Fig. 7 in Appendix A. To establish the phase diagrams of pristine and sonicated CNC, specifically the limits W_0 and W_1, we must start with a CNC suspension that has $W > W_1$ and then dilute this to various lower target concentrations. The pristine suspension can be diluted directly, while the sonicated suspensions must first be concentrated (full details in Appendix D) by transferring to evaporation dishes without spout and monitoring reduction of the volume during stirring. Each concentrated starting suspension was diluted with pure water (Millipore Elix III - Synergy), followed by vigorous shaking and strong vortex mixing for several minutes for homogenization. The final W was established gravimetrically on a four-digit laboratory balance (Sartorius). We filled a fix amount (1 g) of each sample into identical vials (2 mL silanized glass) that were left standing for at least six weeks, sometimes more than one year, to promote macroscopic phase separation in samples within the biphasic regime. Photos of the pristine CNC series are shown in Fig. 7, together with the phase diagram obtained by analyzing the volume fraction of cholesteric to isotropic phase (see Appendix A). In order to increase the precision of the results we established three phase diagrams from each CNC type and averaged.

B. Ultrasonication treatment

Each sample is treated identically using a Hielscher UP200St ultrasonication system model coupled with a 7 mm diameter (at the tip) titanium oscillation immersible horn (sonotrode) S26d7, operating at 26 kHz and a standard amplitude setting of 40% (data from reference experiments at 30% and 50% are in Appendix E). The sonication is done for about one minute to deliver a total energy of 700 J (17.5 J/ml). All sonication parameters were monitored by the device to ensure that the delivered energy is equal for all samples. To prevent overheating, the sonication was done with a 50% time-cycle, and the samples were kept in an ice-water bath throughout the sonication process. For all experiments, vial type and sample amount (40 g) were kept identical, and the sonication tip was always centered within the vial perimeter and immersed to half depth of the liquid. Samples to be sonicated were shaken vigorously but not vortexed prior to sonication. We measured the temperature and conductivity of each sample before and after sonication and found no apparent changes.

C. Characterization

To quantify the fraction of cholesteric phase coexisting with isotropic within the biphasic regime we took pictures of the series of vials prepared with varying W, as described in Appendix A. For estimation of the equilibrium cholesteric helix pitch p we use rectangular capillaries with 4 mm width and 0.4 mm thickness, filled by each suspension using capillary forces. The ends were sealed with two-component epoxy metal glue. The capillaries were left vertical for 1-2 days, and then the bottom liquid crystalline region was imaged using an Olympus BX-51 polarizing microscope in transmission between crossed polarizers. Regions where the helix is in the plane of the capillary exhibit a fingerprint texture with a distance between adjacent lines that is $p/2$. To achieve good statistics, 3–5 images from different locations in the capillary were used and the distance covered by 10 adjacent lines was measured at five regions in every image, the pitch thus extracted as 1/5 of the measured distance. The reported data are

the statistical mean with error bars representing standard error of the mean.

Samples for AFM investigation (Multimode Nanoscope V, Veeco / Bruker) were extracted from vials with $W = 2$ wt.% that had been standing for at least one week and then confirmed between crossed polarizers to be uniformly isotropic. Each source vial was vortexed for 2 min and then a 2 μL aliquot was extracted and diluted with 1 mL of filtered ultrapure water. The diluted suspension was shaken vigorously, followed by the addition of another 1.5 mL of filtered ultrapure water, and the further diluted suspension was vortexed for 2 min. From this mixture 1 mL was transferred in a new vial and diluted with an additional 2 mL of extra-pure water, yielding a final CNC content of 0.00021 wt.%, followed by another 2 min vortex mixing for homogenization and breaking of any CNC chains remaining from higher-concentration suspensions. We then deposited 5 μL of the final diluted suspension onto freshly cleaved mica treated with poly-L-lysine. The liquid droplet was left for 1 min on the substrate, which was then spray-washed with filtered ultrapure water to remove excess suspension and dried with an air gun. The sample was fixed on a metal stub and kept protected from contamination. The amplitude modulation mode was used with a monolithic silicon tip (Tap300Al-G, Nano and More) with radius less than 10 nm and a reflective aluminum coating on the back side. All measurements were performed at ambient temperature. For each W_s, 3–5 AFM scans were performed in different locations.

The AFM data were visualized and analyzed with Gwiddion software (Czech Metrology Institute) v.2.57, giving the possibility of determining the length and thickness of each individual rod. We considered only rods that could be well distinguished as individualized, and always compared images from amplitude and phase scans to avoid rods that are partially or fully overlapped (see details in Appendix E). This process identified about 100-300 individualized CNCs which were measured in each sample to establish the length and thickness distributions.

ACKNOWLEDGMENTS

The authors gratefully acknowledge financial support from the European Research Council under the Horizon Europe Framework Programme/ERC Grant Agreement No. 101167171 (SyG project ALCEMIST). We also thank Evandro Lanzoni, Jonathan Rommelfangen, and Uzair Farooq for technical support with the AFM measurements, and Majdi Assaid for assistance in establishing the phase diagrams.

DATA AVAILABILITY

The data that support the findings of this article are openly available [60].

APPENDIX A: QUANTIFYING PHASE SEPARATION AND ESTABLISHMENT OF THE PRISTINE CNC PHASE DIAGRAM

1. Methodology for quantifying phase separation

For samples in the biphasic window of coexistence of cholesteric LC and isotropic phases, the fact that the LC phase has a higher local CNC mass fraction w_1 than the isotropic phase, with local mass fraction w_0, gives the LC phase higher density than that of the isotropic phase. A vial filled with a biphasic suspension that is left standing vertically will thus experience macroscopic phase separation, with the LC phase gradually sinking down to the bottom of the vial by gravity, unless the CNC content is so high that gelation prevents gravity-driven flow. We utilize this phenomenon to quantify the volume fractions of LC and isotropic phases throughout the biphasic window, and thus establish the phase diagram of a certain series, leaving a set of at least eight vials containing suspensions with increasing global CNC mass fraction W, typically between 1 and 6 wt.%, standing vertically for at least one month.

For the analysis, we slide all vials of a series into a 3D-printed holder from which the vials are hanging from their caps rather than standing on a surface. This prevents the risk

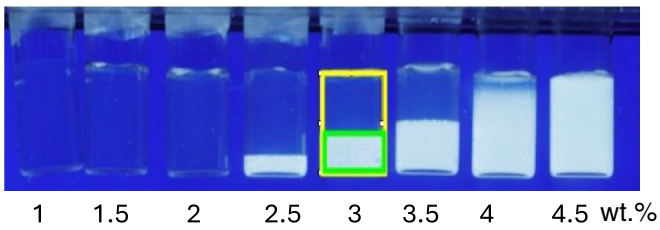


FIG. 6. The volume fraction of liquid crystal phase within the biphasic regime is determined by measuring its height compared to the overall sample height within each vial, after they have been standing sufficiently long for gravity-driven sedimentation to saturate. The process is exemplified here for the $W = 3$ wt.% sample within a series that was sonicated at $W_s = 3$ wt.%

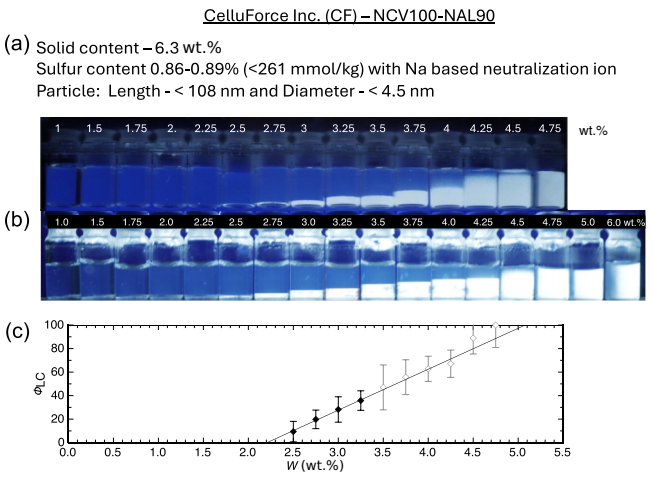


FIG. 7. Characterization of the pristine CNC. (a) Data as provided by the manufacturer CelluForce. (b) Photos of a series of 1 mL vials of the pristine CNC suspension with increasing value of W from left to right, as viewed between crossed polarizers (blueish in character) after one month (top) and one year (bottom), respectively, of standing vertically, to allow any LC phase (appears bright) to sediment to the bottom. (c) The phase diagram established by analyzing the 1-month photo. Filled symbols were used in fitting Eq. (2) while empty ones were not.

that vials fall over during manipulation. The sample holder with all vials is placed between large crossed polarizers in front of a white light source directed horizontally. To photograph all vials simultaneously with high quality, a digital SLR camera (Canon EOS 200D) is placed on the opposite side of the polarizers, oriented along the normal to the planes of the light source, polarizers, and vial series—all of which are oriented parallel to each other—to avoid visible parallax deformations. Since the isotropic phase is not birefringent, it appears dark between crossed polarizers. In contrast, the LC phase appears bright due to its birefringence. In order that we are still able to distinguish the liquid–air surface and thus establish the overall liquid height in a vial, we either use polarizers with a blueish dark state or we insert a birefringent foil that gives a violet dark state (the latter option was used when filming the videos). An example photo is shown in Fig. 6.

We analyze the photos with the software Fiji (Image J, Source Forge project), setting the correspondence between image pixel and horizontal dimension of a vial (all vials are identical) to 10 units. Then a rectangle is drawn approximately about the whole liquid volume, shown in yellow in Fig. 6. The width is not important as only the height is analyzed. A smaller rectangle is drawn around the bright LC fraction, as shown in green. By dividing the height of the green rectangle by that of the yellow, we obtain the LC volume fraction ϕ_{LC} for a sample, after which both rectangles are moved to the next vial in the image, and the process is repeated. The main systematic uncertainty is due to the adjustment of the rectangle bottoms, complicated by the deviation from a perfect flat bottom of the vials, and tops, complicated by the slight meniscus curvature at the liquid–air interface. The meniscus curvature is minimized by the use of silanized glass for the vials. By ensuring sufficient filling of each vial, the impacts of both uncertainties are kept low. For samples where w_1 is approaching or even surpassing w_k, e.g., the $W = 4$ wt.% sample in Fig. 6, a further problem is the impact of gelation, which renders a truly reliable measurement of ϕ_{LC} impossible. Such data must thus be interpreted with care, as we discuss in more detail below.

2. The pristine CNC suspension phase diagram

Relevant data on the commercially obtained CNC provided by the manufacturer (CelluForce) are summarized in Fig. 7(a) as well as in the benchmarking paper [61] by the Cranston group. When dealing with experimentally determined parameter values, we must distinguish between values of the pristine and of sonicated suspensions, which are often not the same. For this reason, we add an asterisk to parameters that apply specifically to the pristine CNC suspension. To establish the stability limits of the isotropic and cholesteric phases for the pristine suspension, W_0^* and W_1^*, respectively, we prepare sixteen vials with identical volumes of CNC suspension, each one diluted from the original slurry to different selected CNC mass fractions in the range $W = 1.0 - 5.0$ wt.% (see Section V for experimental details).

Since $W_1^* > w_k$ we cannot establish W_1^* directly in the experiment. To circumvent this problem, while also establishing W_0^* with greater accuracy, we measure the apparent volume fraction Φ_{LC} of cholesteric phase after one month of sedimentation in all samples of the pristine suspension, plot the data versus W, and fit Eq. (2) to those data points in the biphasic regime that follow a linear or sublinear trend, see Fig. 7(c). We exclude high-W data points that follow a superlinear trend, because the CNC dispersity and LC formation-driven fractionation should give a sublinear behavior since the isotropic phase has monotonically decreasing average L_e/D_e as $W \to W_1^*$ within the biphasic regime. Superlinear points reflect a state where the apparent LC phase is actually a percolated network of gelled LC subvolumes ($w_1 \geqslant w_k$), trapping isotropic droplets that cannot rise to the top along gravity and thus producing apparent Φ_{LC} values that are too high. We extract as fitting parameters the values $W_0^* = 2.2$ wt.% and $W_1^* \approx 5.1$ wt.%. Both W_1^* and w_k must be interpreted as rather rough estimates since neither parameter is directly experimentally accessible when $W_1^* > w_k$.

APPENDIX B: CONSIDERATION OF HOW TO APPLY ONSAGER THEORY RESULTS TO CNC SUSPENSIONS IN PRACTICE

In the Onsager approximation of nondisperse rods, the width of the biphasic regime is $\Delta\phi = \phi_1 - \phi_0 = 1.2D_e/L_e \approx 0.36\phi_0$. For electrostatically stabilized nanoparticles like CNCs, the effective diameter D_e can be approximated as the sum of an average of the breadth B and thickness T of the core particle and the electrostatic screening from the surface, which is quantified by the Debye length l_D: $D_e = (B + T)/2 + 2l_D$. Analogously, the effective length L_e is $L_e = L + 2l_D$. Since l_D depends on the ionic strength, which in turn depends on the surface charge and number of CNCs in suspension, the ratio between the effective CNC volume fraction ϕ and the mass fraction W changes with varying W, which is the experimentally accessible parameter [39]. It is thus impractical to work with ϕ in experiments, and instead we define the stability limits of the isotropic and nematic (or cholesteric) phases as critical mass fractions W_0 and W_1 corresponding to ϕ_0 and ϕ_1, respectively. We use lower case w for the *local* mass fraction in a uniform subvolume within a phase-separated sample, while upper case W is used for denoting the global CNC mass fraction of the overall suspension, uniform or phase-separated. We must make this distinction because at equilibrium within the biphasic regime (but not at its borders W_0 and W_1), we have $w \neq W$ at every location in the sample due to the spontaneous phase separation into coexisting isotropic and nematic phases with nonequal w.

Contrary to the idealized case of nondisperse straight nanocylinders that Onsager considered, most nanoparticles, including CNCs, are highly disperse and they are not perfect cylinders. The phase separation in the biphasic regime then leads to a localized fractionation [32,34,35] where the CNCs with highest L_e/D_e form the first tactoids after equilibration at W just above W_0^*. While the value W_0^* is thus dominated by the highest aspect-ratio CNCs, the last remaining isotropic phase at the end of the biphasic regime has a low average L_e/D_e, yielding a W_1^* of the global disperse suspension with a rather high value, much greater than the $W_1 = 1.36W_0^*$ that would be expected from Onsager theory for nondisperse particles (ignoring the dependence of l_D on ionic strength).

As a first striking consequence, the actual observed biphasic regime width ΔW^* of a pristine CNC suspension is thus much wider than $0.36W_0^*$. Indeed, with $W_0^* \approx 2.2$ wt.% and $W_1^* \approx 5.1$ wt.%, our pristine CNC suspension has a large $\Delta W^* \approx 1.3W_0^*$.

A second important consequence of the dispersity and the spontaneous fractionation of the highest aspect ratio CNCs into tactoids is that the local w_0 and w_1 continuously increase with increasing W within the biphasic regime, thus deviating from the globally determined values W_0 and W_1. These are valid only at the lower and upper boundary, respectively. Based on Onsager theory, we may estimate the limiting local value pairs at the boundaries of the biphasic regime as $w_0 = W_0$ and $w_1 \approx 1.36w_0$ at the lower boundary, and $w_1 = W_1$ and $w_0 \approx w_1/1.36$ at the upper boundary. For the quantitative analysis of any observations taken in the LC phase fraction of samples in the biphasic regime, such as the cholesteric helix pitch p, we need to estimate the nematic phase CNC mass fraction w_1 also in the intermediate regime. To this end we use a simple heuristic interpolation as a function of global CNC mass fraction W:

$$w_1 \approx W\, 1.36^{\frac{W_1 - W}{W_1 - W_0}}. \tag{B1}$$

Here W_0 and W_1 are the boundaries of the biphasic regime of a particular CNC suspension as determined on macroscopic samples. By inserting $W = W_0$ and $W = W_1$, respectively, it is clear that the interpolation correctly produces the borderline values of w_1. When applying Eq. (B1) to the pristine CNC, $W_0 = W_0^*$ and $W_1 = W_1^*$, but for sonicated CNC the W_0 and W_1 values can differ strongly, as shown in the main paper.

APPENDIX C: VISCOSITY OF PRISTINE AND SONICATED CNC SUSPENSIONS

Figure 8 shows the results of microfluidic viscosity measurements on the pristine CNC sample at four representative mass fractions W, as well as on the resulting suspensions after sonicating at mass fractions W_s with the same four values. The long-range order in LCs means that a nematic phase has no less than five different viscosities [50]. However, when no particular precautions are made to align the LC, as in our case, the effective shear viscosity that is typically experienced in a flow-aligned sample is the lowest viscosity, η_2, corresponding to flow along **n**.

The effective viscosity increases monotonically for all samples with increasing W, but for $W \geqslant W_0^*$, this tendency is much more pronounced at low flow rates; as $W \to W_1^*$, low flow rates yield very high effective viscosity, while rates greater than about 50 μL/min bring it down to a low value range in which the dependence on W is rather small. This reflects the increasing fraction of equilibrium liquid crystal phase as $W \to W_1^*$ as well as the fact that this fraction exhibits a high apparent viscosity if **n** is not along the direction of flow; this is the case at low flow rate, where **n** rotates within the cholesteric helix, which initially has random orientation. Beyond ∼50 μL/min flow rate, however, the helix axis **m** is expected to align along the shear gradient [56] and the helix also starts unwinding, with **n** predominantly along the flow. We therefore measure a low effective viscosity that approaches η_2 as the helix is increasingly unwound.

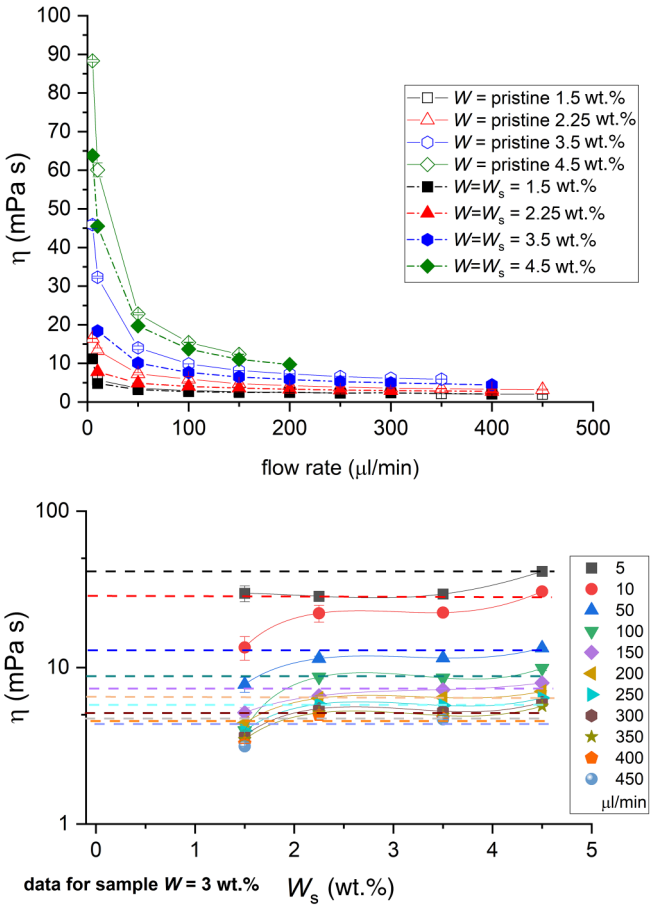


FIG. 8. (a) Viscosity evolution with increasing flow rate for suspensions sonicated at four different W_s (filled symbols, dashed lines) compared to the pristine nonsonicated suspensions at the corresponding W (empty symbols, continuous lines). (b) Impact of W_s on viscosity at different flow rates, when each sample has been tuned after sonication to $W = 3.0$ wt.%. As a reference, the viscosities of the pristine nonsonicated suspension are indicated with horizontal dashed lines.

At the highest studied values of W, the vicinity to w_k may add further to the apparent viscosity. For $W < W_0^*$, in contrast, the sample is isotropic at rest but the flow can produce a paranematic state where **n** is born aligned along the flow, yielding η_2 as the effective viscosity almost irrespective of flow rate. At $W \approx W_0^*$, the pristine and sonicated data are rather similar regardless of flow rate, but as $W \to W_1^*$, we find a decrease of effective viscosity after sonication, the difference being the greatest at low flow rates. Sonicated samples are thus more easily flow-aligned than the pristine samples at the same W, an observation that corroborates the observation that all samples sonicated in the range $W_s \leqslant 3.0$ wt.% appear isotropic at rest after sonication while a paranematic state is easily flow-induced.

APPENDIX D: PHASE DIAGRAMS OF SONICATED CNC SUSPENSIONS

In order to establish the phase diagrams of sonicated CNC, we have to upconcentrate each sample where $W_s < W_1$ such

TABLE I. CNC mass fraction after upconcentration (right column) as a function of CNC mass fraction during sonication, W_s (left column), in order to establish phase diagrams.

W_s (wt.%)	W after upconcentration (wt.%)
1.0	6.3
1.5	5.2
1.75	5.9
2.0	4.9
2.25	4.9
2.5	7.4
2.75	7.4
3.0	7.3
3.25	7.9
3.5	6.3
3.75	6.9
4.0	4.9
4.25	6.9
4.5	6.0
4.75	5.3
5.0	5.3
6.0	7.4

that we can prepare subsamples over a range of W-values. The process of upconcentration is difficult to control accurately, as it takes place by evaporation over many days, but we measure the final CNC mass fraction in each sample, as summarized in Table I. Concentrated suspensions were transferred to a closed flask and stored in a fridge (4°C) until use. Prior to use (mainly to establish phase diagrams), we let the sample adopt room temperature, we homogenize it, and measure its total mass concentration W.

For each value of W_s, we prepare vials at different W to establish the phase diagram, following the procedure described in Appendix A. The photos of suspension series between crossed polarizers as well as the extracted phase diagrams are summarized in Fig. 9. The data for the series sonicated at $W_s = 1.0$ wt.% were not included in Figs. 3(b) and 3(c) in the main paper, because the established phase diagram is clearly false. This is because W_0 is quite high, between 2.5 and 3.0 wt.%, and W_1 must be so high as to induce complete sample gelation even at modest Φ_{LC}. The increase in Φ_{LC} from $W = 3.0$ to $W = 3.5$ wt.% is very small for this series, yet at $W = 4.0$ wt.% the vial is fully gelled. We can thus conclude that W_0 and W_1 are even greater after sonication at $W_s = 1.0$ wt.% than the maximum respective values plotted in Fig. 3(c) even though we cannot give values reliable enough to include in the diagram. As discussed in the main paper, many of the other phase diagrams are also not trustworthy, as a result of the upconcentration required to establish the phase diagrams, and therefore, we selected only three phase diagrams for sonicated CNCs that were deemed reliable in Fig. 3(a) in the main paper.

APPENDIX E: ANALYSIS OF AFM DATA

1. Distinguishing individual from agglomerated CNCs

The samples prepared for AFM investigation (see Sec. V for procedure) were measured over a square area with side length 3 μm (512x512 resolution) using a Veeco/Bruker Multimode Nanoscope V AFM. To increase precision, measurements (scans) were performed in 5 or more places for each sample (pristine CNC and CNC suspensions sonicated at varying W_s). The AFM measurements were performed in tapping mode, where the amplitude and frequency signals from tip oscillation depend on the tip interaction with the sample surface. It is well known that the resolution of AFM is poorer in the lateral than in the vertical direction due to an effect called tip convolution: when the tip passes over the edge of an object in the nanometer range, such as CNCs, the non-zero size of the tip affects the data which are smeared out. For this reason, we use the height data (z direction) for quantifying the lateral dimension of CNCs.

An example of a sample area with the three main kinds of CNC bundles (see Fig. 4) is shown in Fig. 10. A quantitative analysis was performed using the software Gwyddion, which allows different modes of visualizing the data. The amplitude signal constructs the height image (Fig. 10, left and top right) which shows protrusions from the substrate as a function of location by varying brightness according to the color scale. In many cases objects with large z extension (high brightness) consist of partially or fully overlapped CNCs, hence their height does not reflect the breadth B or thickness T of an individual CNC. The *phase* image (Fig. 10, bottom right) is obtained from the frequency signal's shift. While dimensions cannot be measured from this image, it is more effective in distinguishing agglomerated from individual CNCs, for instance, via "shadows" along individual CNCs within a bundle.

The crossed CNC bundles are easily distinguished in either image type due to their unambiguous geometrical features. Bundles of side-to-side-agglomerated CNCs can be subdivided into two categories, depending on whether the agglomeration is within (xy plane) or perpendicular (z direction) to the substrate plane. The first ones can be recognized particularly well in the phase image by the shadow between the individual CNCs. As an example, the bundle labelled 1 in the height image, where it appears to be a single object, actually consists of the side-to-side agglomerated CNCs labeled 1a and 1b in the phase image, distinguished by the dark shadow between them. The same holds for bundle 4 in the height image.

The bundles of vertically stacked CNCs are best recognized by their z obtained from the height image. Since it is very unlikely that the individual CNCs in the bundle have the exact same length, there will be regions near the ends of the bundle where the height suddenly appears to double; this is too large and too sudden a change in thickness to be attributed to a single CNC, and thus we interpret this as a sign of a vertical bundle. Sometimes the vertical stacking is visible directly, as for particle 6. End-to-end-connected CNCs form a long chain that can often be weakly distinguished already in the height image (particles 2 and 3 in Fig. 10 appear weakly connected), and in the phase image, it is clear that the substrate is not visible at any point between them. In many cases, there is a combination of different kinds of agglomeration.

After identifying the individual CNCs, their length L and thickness T were obtained from the height image of each sample. A line was drawn manually along the length of

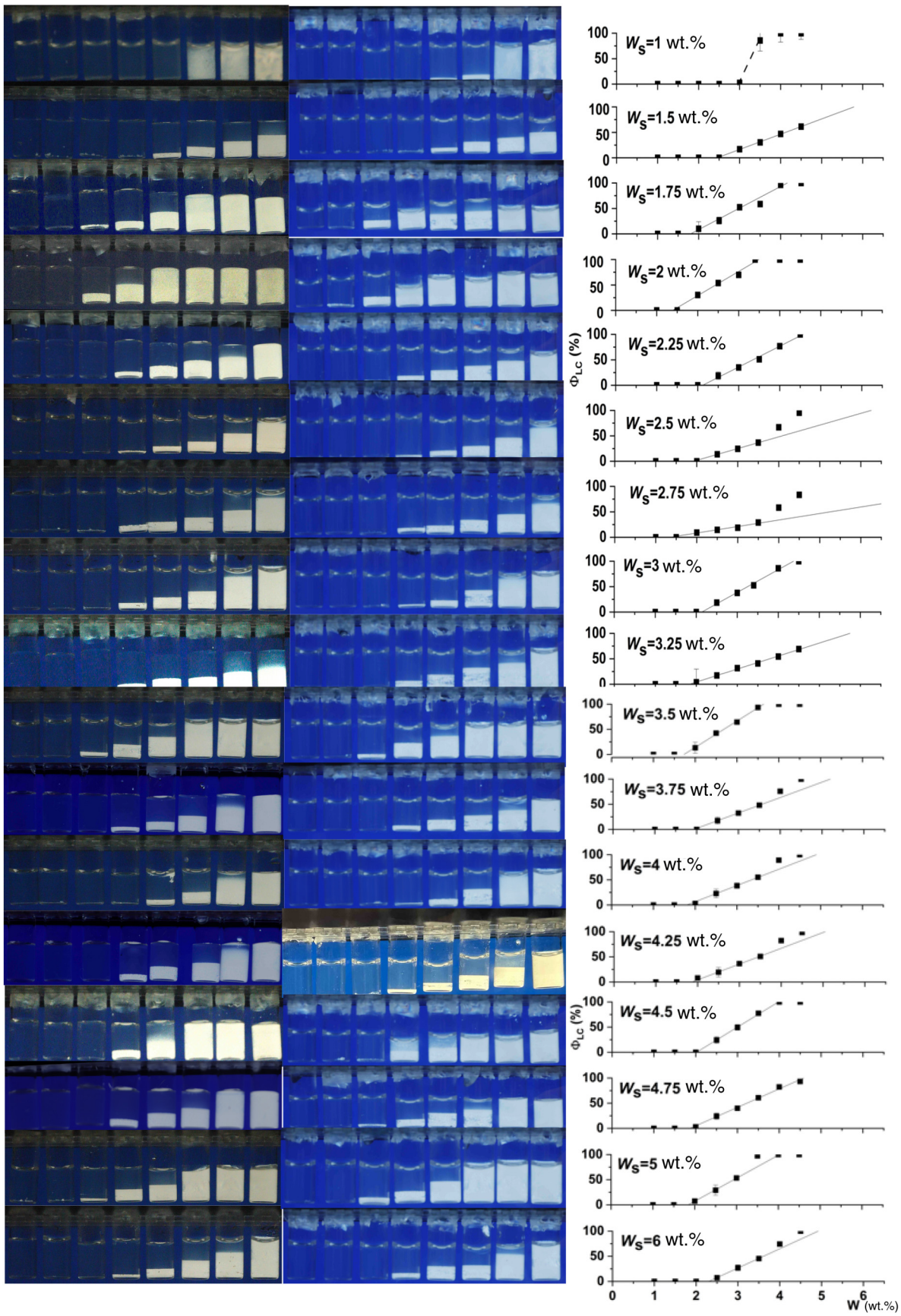


FIG. 9. Phase diagrams after sonication. Left and middle column: photos of equilibrated vials with varying W, for the pristine CNC as well as for all values of W_s studied, after six weeks (left) and after one year (middle). Right column: phase diagrams as established by fitting Eq. (2) to the experimental data extracted from the photos after six weeks.

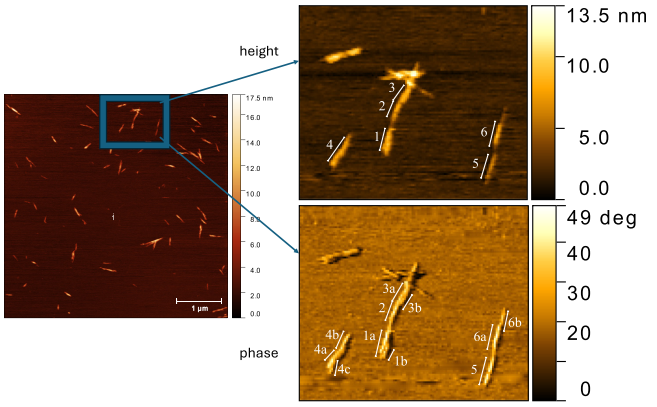
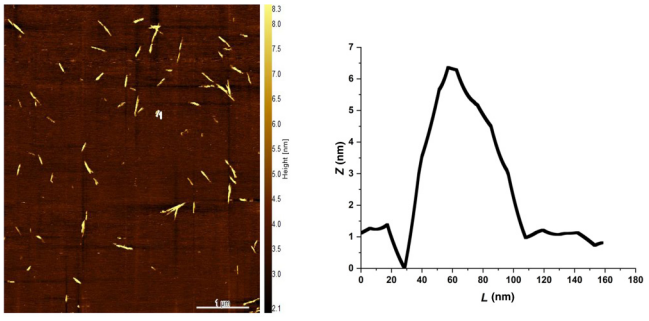


FIG. 10. Examples of AFM height and phase images from the same sample, illustrating how one can distinguish between individualized and agglomerated CNCs.

each selected CNC, and L was estimated by applying the Pythagorean theorem to the projections on the x and y axes, see Fig. 11. To estimate T, the drawn line was moved along the length of the rod until it touches the background (mica), and the program gives the difference between the minimum and maximum z-values along this line as Δz. We use this value for T, cautioning that an artifact-free data point represents the *maximum* thickness along the CNC, but artifacts with exaggerated T values may arise in case a CNC is kinked or twisted. The former may raise local sections of the CNC from the substrate, while the latter could bring the breadth B instead of the thickness T locally into the z direction.

2. Fitting the correct distribution function to statistical data from the AFM analysis

For the pristine CNC we estimate the size of 248 rods analyzed following the above procedure, and for the sonicated CNCs, the number of rods varied over the range 100–300 for



$L = \sqrt{(\Delta x)^2 + (\Delta y)^2}$ $T = Z_{max}$

Δx (μm)	Δy (μm)	L (μm)	T (nm)
0.060	0.067	0.090	5.107

FIG. 11. The CNC length L is estimated by applying the Pythagorean theorem to the projections on the x and y axes. The lateral dimension T is estimated automatically from the vertical distance to the ground level, which is the level of the mica substrate. The example is from an AFM image for $W_s = 2.25$ wt.%.

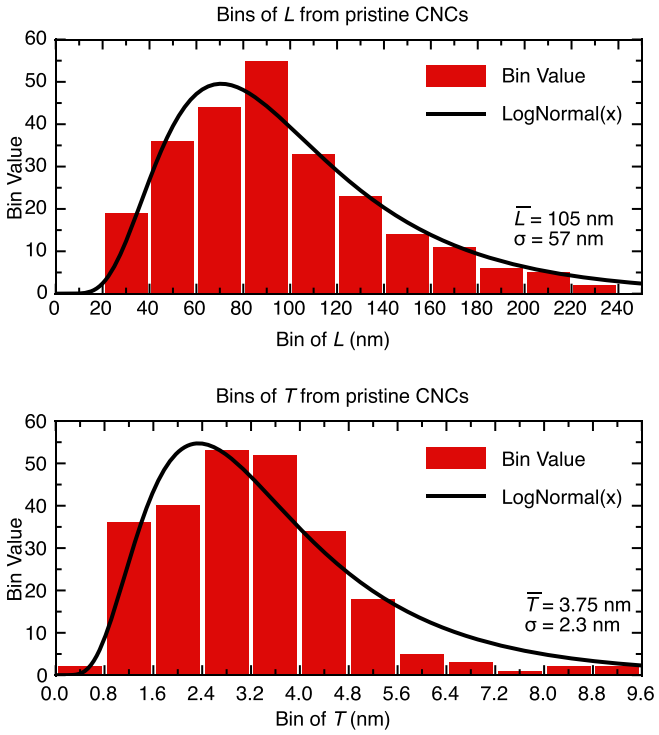


FIG. 12. Histograms and log-normal fits for length and thickness data obtained from AFM on the pristine CNC.

each W_s. To establish average lengths $\bar{L}$ and thicknesses $\bar{T}$ for the pristine and each sonicated CNC, the individual CNC data were binned into suitable bands (see below), the number in each bin converted to its percentage of all the CNCs, and a log-normal function was fitted to the data using mainly the software Pro Fit (Quantumsoft) but also Origin (OriginLab) was used for reference. We use the notation of Origin for the fitting parameters, with X_c and ω referring to the logarithm of the parameter of interest, not to the parameter itself. To obtain the mean $\overline{X}$ and standard deviation σ_X of the parameter X (which is replaced by the length L or the thickness T, as appropriate), the following formulae apply:

$$\overline{X} = \exp\left(\ln X_c + \omega^2/2\right) \tag{E1}$$

and

$$\sigma_X = \overline{X}\sqrt{\exp\left(\omega^2\right) - 1}. \tag{E2}$$

The corresponding histograms, fitted log-normal functions and the resulting $\overline{X}$ and σ_X are shown in Fig. 12 for the pristine CNC and in Figs. 13 and 14 for the suspensions sonicated at 40% amplitude. The data for 30% and 50% amplitude can be found in the data repository for the article.

It is nontrivial to establish the appropriate bin number for skewed distributions such as the lognormal, which we are dealing with here. As a first guide, we use Doane's formula (see, e.g., [62]) to establish the number of bins $\hat{k}$:

$$\hat{k} = 1 + \log_2(n) + \log_2\left(1 + \frac{|g_1|}{\sigma_{g_1}}\right), \tag{E3}$$

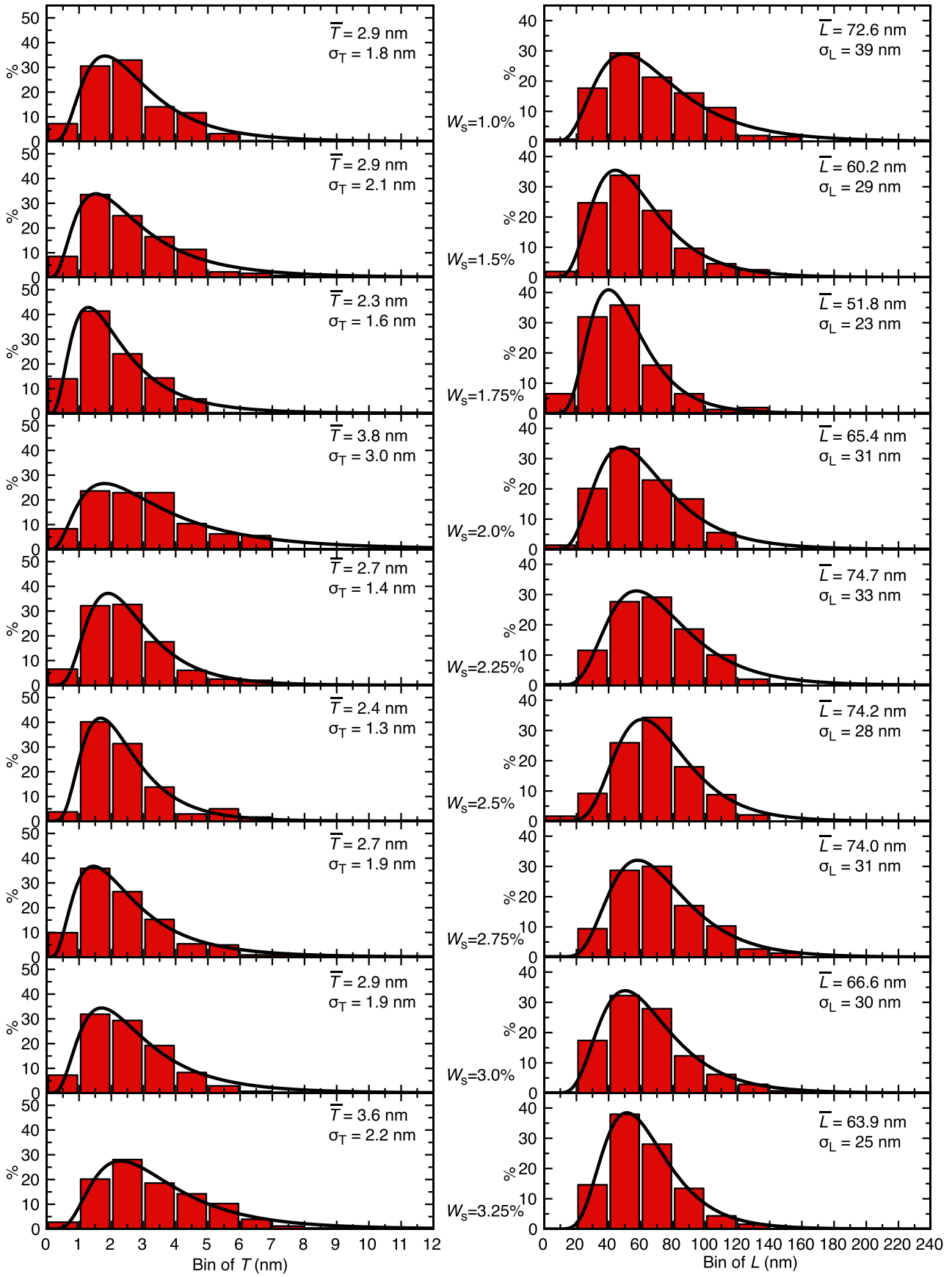


FIG. 13. Histograms and log-normal fits for length L and thickness T data obtained from AFM for CNC suspensions sonicated at 40% amplitude at varying W_s, part 1. The mean values $\overline{T}$ and $\overline{L}$ as well as the corresponding standard deviations σ_T and σ_L, as obtained using Eqs. (E1) and (E2) on the fitted parameters X_c and ω are indicated in each diagram.

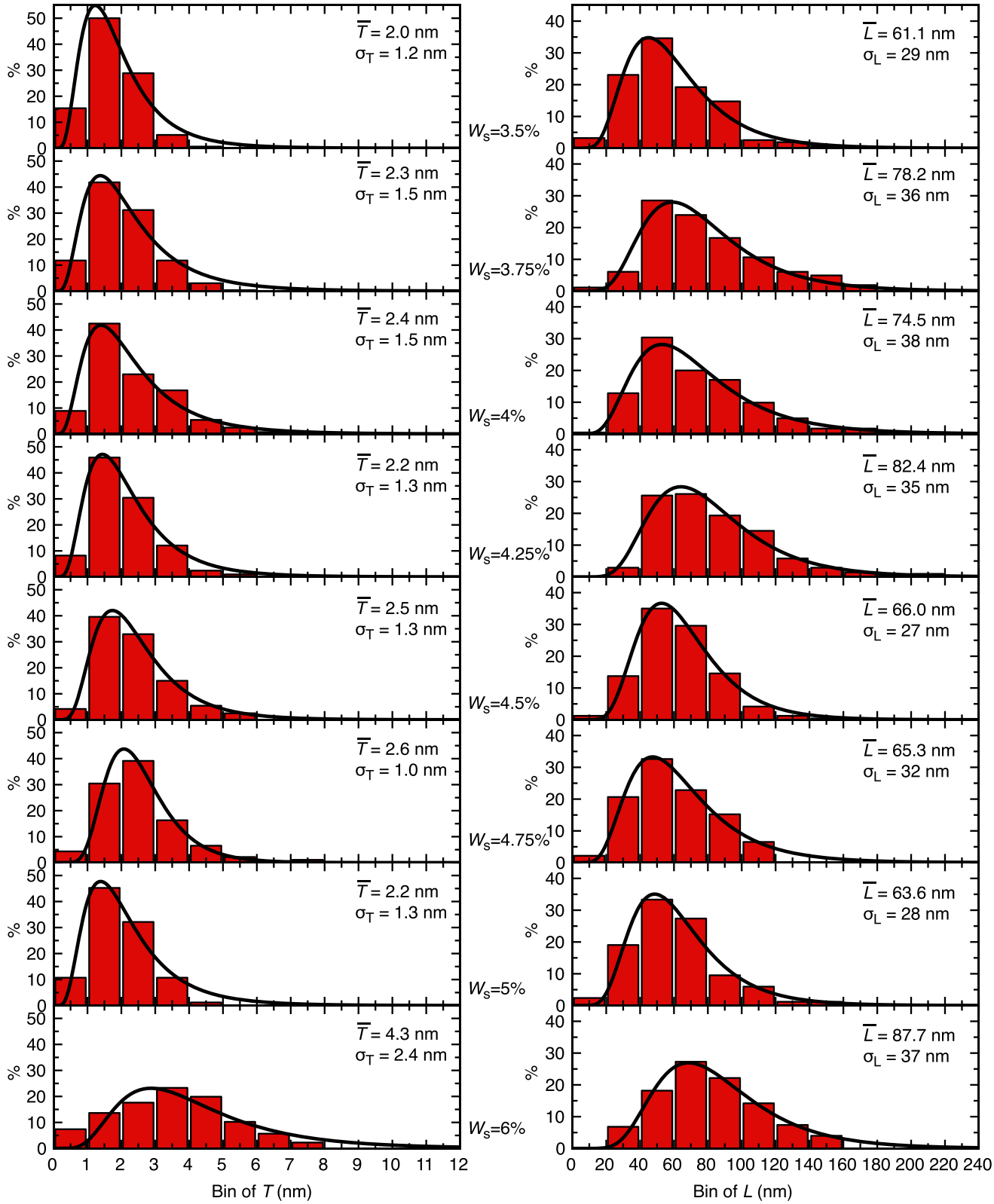


FIG. 14. Histograms and log-normal fits for length L and thickness T data obtained from AFM for CNC suspensions sonicated at 40% amplitude at varying W_s, part 2. The mean values $\overline{T}$ and $\overline{L}$ as well as the corresponding standard deviations σ_T and σ_L, as obtained using Eqs. (E1) and (E2) on the fitted parameters X_c and ω are indicated in each diagram.

where n is the number of measurements in the sample and the moments estimator g_1 and its variance $\sigma^2_{g_1}$ are defined as

$$g_1 = \frac{\frac{1}{n}\sum_{i=1}^{n}(x_i - \bar{x})^3}{\left[\frac{1}{n}\sum_{i=1}^{n}(x_i - \bar{x})^2\right]^{3/2}} \tag{E4}$$

and

$$\sigma^2_{g_1} = \frac{6(n-2)}{(n+1)(n+3)}. \tag{E5}$$

Applying Doane's formula to the pristine CNC, where we have $n = 248$ individual measurements and $\overline{L} = 95.0$ nm and $\overline{T} = 3.16$ nm, we first obtain for L:

$$g_1 = \frac{\frac{1}{248}\sum_{i=1}^{n}(x_i - 95)^3}{\left[\frac{1}{248}\sum_{i=1}^{n}(x_i - 95)^2\right]^{3/2}} = 0.73975 \tag{E6}$$

and

$$\sigma_{g_1} = \sqrt{\frac{6(246)}{(249)(251)}} = 0.15368, \tag{E7}$$

which yields a recommended bin number of

$$\hat{k} = 1 + \log_2(248) + \log_2\left(1 + \frac{0.73975}{0.15368}\right) = 11.5. \tag{E8}$$

With $L_{\min} = 21$ nm and $L_{\max} = 233$ nm we need to cover the range 20–240 nm, hence we obtain a recommended bin width of $220/11.5 = 19.1$ nm. We approximate this to 20 nm, yielding 11 bins with centers from 30 to 230 nm. In the top diagram in Fig. 12, we let the x-axis start at $L = 0$ for clarity, but there is no bin at 10 nm, since there are no data points there.

The same calculation for T gives a recommended bin number of $\hat{k} = 11.96$. With $T_{\min} = 0.3$ nm and $T_{\max} = 9.6$ nm we obtain a practical bin width of 0.8 nm for the thickness data, which we plot with 12 bins centered from 0.4 to 9.2 nm in the bottom diagram in Fig. 12.

For the sonicated suspensions, the establishment of bin numbers and limits is complicated by the fact that we wish to be able to compare L and T data obtained at different W_s, and an analysis by Doane's formula of each individual data set typically yields slightly different results. In the repository published with this article is a file showing all the results, where we see that $\hat{k}$ for both parameters falls in the range 9–13. The optimum choice of bin numbers also needs to consider the lower and upper limits of the data, such that the bins represent reasonably convenient values, for all data sets that should be visualized together. For T the data range from just over 0 to 11.7 nm in an extreme case, while for L, the range is 6–222 nm. Compiling these observations, we choose 12 bins for T from 0 to 12 nm, with a constant 1 nm distance, centered over 0.5 nm for the first bin to 11.5 nm for the last one. For L, our choice is to work with 12 bins with 20 nm distance, at centers from 10 to 230 nm.

3. Lengths and thicknesses of CNCs sonicated at different amplitudes

In addition to the AFM results shown in Fig. 2, obtained on CNC suspensions sonicated at 40% amplitude, we did the same analysis for suspensions sonicated at 30% and 50% amplitude as well, see Fig. 15.

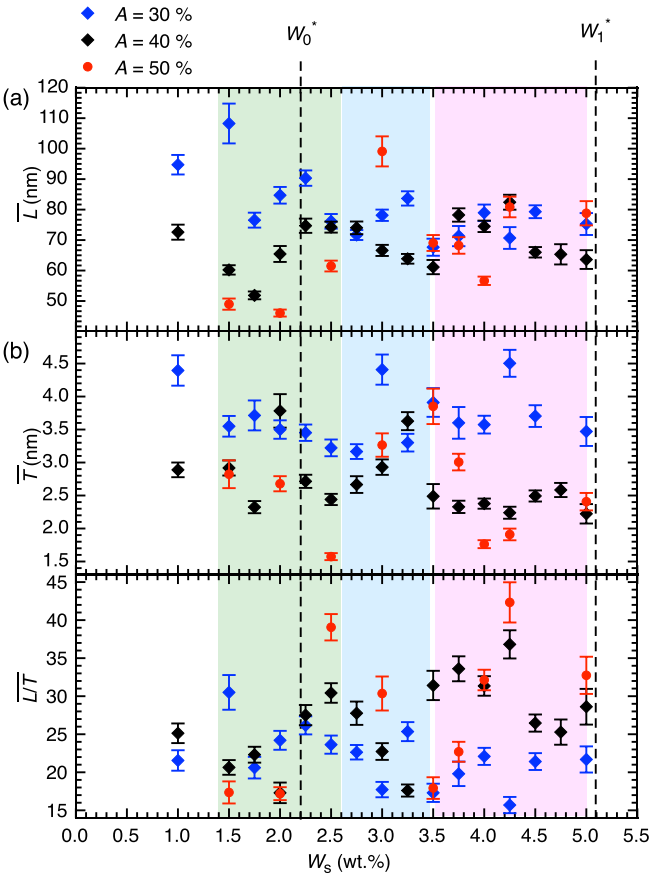


FIG. 15. Impact of W_s on individualized CNC average length $\overline{L}$ (a), average thickness $\overline{T}$ (b), and average aspect ratio $\overline{L/T}$, for sonication amplitudes from 30% to 50%. The data for 40% are identical to those in Fig. 2. The sample sizes and applied energies are identical for all amplitudes. Error bars represent the standard error of the sample mean, $\sigma_{\overline{L}} = \sigma_L/\sqrt{n}$ and $\sigma_{\overline{T}} = \sigma_T/\sqrt{n}$, i.e., they represent the confidence in establishing each mean value, not the dispersity of the suspension. Note that all CNCs that are deemed to be part of a bundle are excluded.

APPENDIX F: INFLUENCE OF SONICATION ON CHOLESTERIC HELIX PITCH

The cholesteric helix pitch was established from the POM texture photos in Fig. 16, taken in capillaries that had been standing vertically for sufficient time for equilibration, as described in the Methods section.

APPENDIX G: DESCRIPTION OF SUPPLEMENTAL VIDEOS

(1) Supplemental Video 1 [49] is the source of the still images in Fig. 1. The video is a compilation of multiple videos, each one showing the response of a CNC suspension to sonication as visualized by placing the vial between crossed polarizers with a white backlight on the side opposite of the camera, and a birefringent foil between vials and the polarizer closest to the camera which approximates the function of a

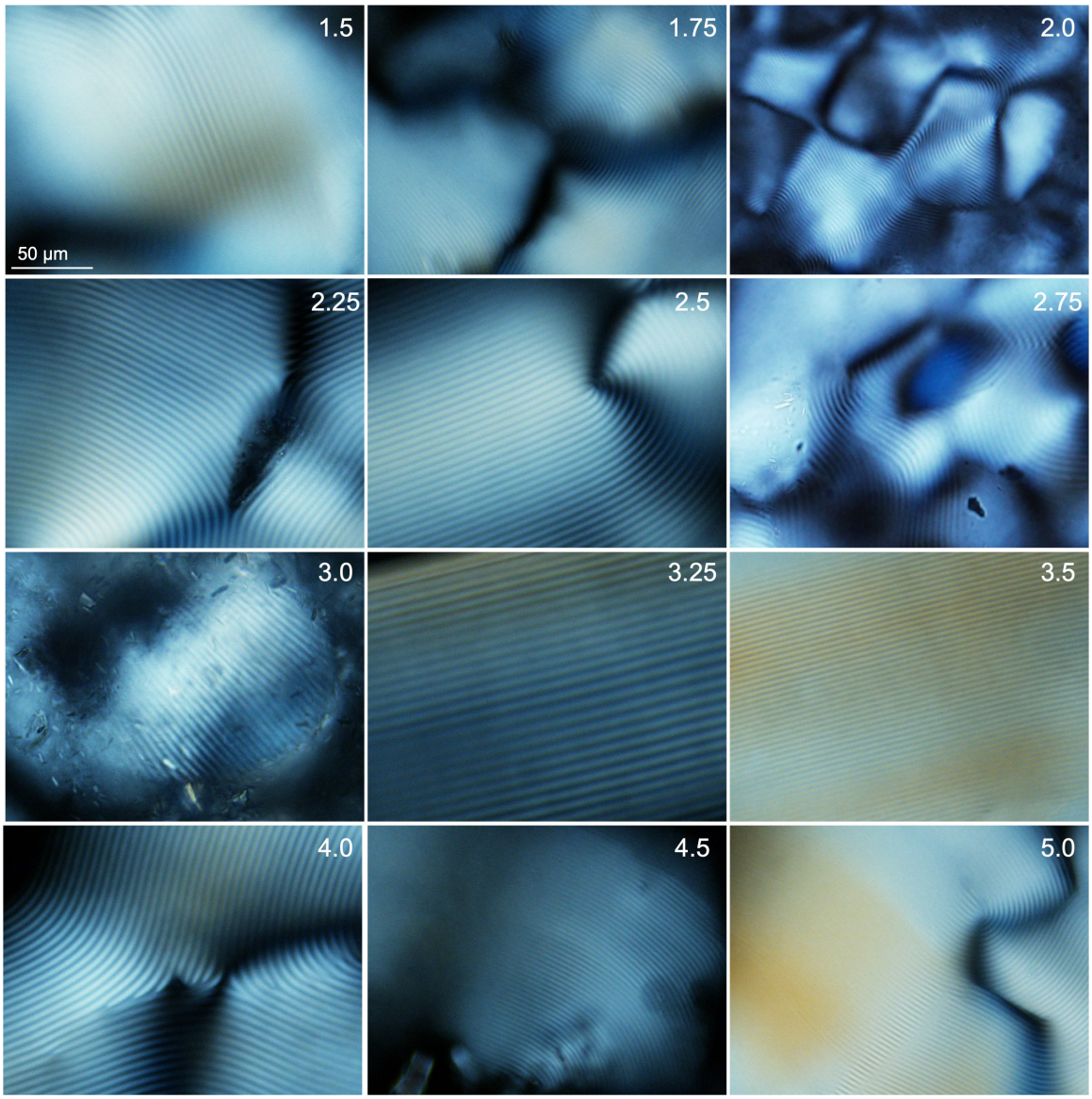


FIG. 16. Representative texture photos from which the cholesteric helix pitch data were measured, one example for each of the values in Fig. 3(c). The images are taken using samples with $W = 3$ wt.% between crossed polarizers. The 50 μm scale bar in the top left image is valid for all other images as well.

first-order λ phase plate. W_s increases from left to right as indicated along the top. The video is real-time and it is filmed with 25 frames/s. The black rod inserted from the top is the sonotrode tip; the top of each sample is the air interface and the bottom is the vial bottom. At the end of the video, we show the samples 19 days later, during which they have been standing still and untouched, with the same imaging conditions. The sonication tip is gently inserted, moved around a bit, and then extracted, to show the appearance of shear-induced paranematic state. Spontaneous formation of cholesteric LC phase can be seen in the vials with $W_s \geqslant 2.5$ wt.%. Due to its higher density, it has sedimented towards the bottom of each vial.

(2) Supplemental Video 2 [49] shows vials with $W_s =$ 1.75, 2.0, and 2.25 wt.%, prepared in the same way as the vials in Supplemental Video 1, which go through the same 1-minute sonication procedure as in Video 1 but this time we film the initial insertion of the sonication tip into the vial before the sonication starts. Then we see the entire sonication process followed by brief relaxation and extraction of the tip, and finally the tip is reinserted in the freshly sonicated vial. Comparing the beginning and end of the video it is striking how much stronger the shear-induced paranematic birefringence during tip insertion is before than after sonication. The imaging conditions are identical to those in video 1.

(3) Supplemental Video 3 [49] shows six vials of CNC suspension, two each with $W = 1.75$, 2.0, and 2.25 wt.%. All are based on suspensions that were sonicated in the same way as in Supplemental Video 1 at W_s identical to the current W, but after sonication, one of each W value was upconcentrated to $W = 4.9$ wt.% and one was upconcentrated to $W = 5.6$ wt.%. All were then diluted again to their original W. During the movie, a metal rod is slowly inserted into each vial

and then pulled back out, to demonstrate paranematic order generation and the relaxation after the motion has stopped. The video is a compilation of six individual videos, cropped and placed side by side in order to allow direct comparison. The $W = 2.0$ and 2.25 wt.% vials prepared by diluting the $W = 5.6$ wt.% suspension have strong static birefringence and lack smooth flow response. Imaging conditions are identical to those in Video 1.

[1] J. Taurozzi, V. Hackley, and M. Wiesner, Ultrasonic dispersion of nanoparticles for environmental, health and safety assessment–issues and recommendations, Nanotoxicology **5**, 711 (2011).

[2] D. Y. Hoo, Z. L. Low, D. Y. S. Low, S. Y. Tang, S. Manickam, K. W. Tan, and Z. H. Ban, Ultrasonic cavitation: An effective cleaner and greener intensification technology in the extraction and surface modification of nanocellulose, Ultrason. Sonochem. **90**, 106176 (2022).

[3] I. Sondi, D. Goia, and E. Matijević, Preparation of highly concentrated stable dispersions of uniform silver nanoparticles, J. Colloid Interface Sci. **260**, 75 (2003).

[4] N. Mandzy, E. Grulke, and T. Druffel, Breakage of TiO_2 agglomerates in electrostatically stabilized aqueous dispersions, Powder Technol. **160**, 121 (2005).

[5] Y. Y. Huang and E. M. Terentjev, Dispersion of carbon nanotubes: Mixing, sonication, stabilization, and composite properties, Polymers **4**, 275 (2012).

[6] A. Gedanken, Using sonochemistry for the fabrication of nanomaterials, Ultrason. Sonochem **11**, 47 (2004).

[7] G. Nyström, M. Arcari, and R. Mezzenga, Confinement-induced liquid crystalline transitions in amyloid fibril cholesteric tactoids, Nat. Nanotechnol. **13**, 330 (2018).

[8] A. Narkevicius, R. Parker, J. Ferrer-Orri, T. Parton, Z. Lu, G. van de Kerkhof, B. Frka-Petesic, and S. Vignolini, Revealing the structural coloration of self-assembled chitin nanocrystal films, Adv. Mater. **34**, 2203300 (2022).

[9] B. Frka-Petesic, T. G. Parton, C. Honorato-Rios, A. Narkevicius, K. Ballu, Q. Shen, Z. Lu, Y. Ogawa, J. S. Haataja, B. E. Droguet, R. M. Parker, and S. Vignolini, Structural color from cellulose nanocrystals or chitin nanocrystals: Self-assembly, optics, and applications, Chem. Rev. **123**, 12595 (2023).

[10] D. Klemm, F. Kramer, S. Moritz, T. Lindström, M. Ankerfors, D. Gray, and A. Dorris, Nanocelluloses: A new family of nature-based materials, Angew. Chem. Int. Ed. **50**, 5438 (2011).

[11] Y. Habibi, L. Lucia, and O. J. Rojas, Cellulose nanocrystals: Chemistry, self-assembly, and applications, Chem. Rev. **110**, 3479 (2010).

[12] J. P. Lagerwall, C. Schütz, M. Salajkova, J. Noh, J. H. Park, G. Scalia, and L. Bergström, Cellulose nanocrystal-based materials: From liquid crystal self-assembly and glass formation to multifunctional thin films, NPG Asia Mater. **6**, e80 (2014).

[13] W. Hao, M. Wang, F. Zhou, H. Luo, X. Xie, F. Luo, and R. Cha, A review on nanocellulose as a lightweight filler of polyolefin composites, Carbohydr. Polym. **243**, 116466 (2020).

[14] L. Müller, A. Zingg, A. Arcifa, T. Zimmermann, G. Nyström, I. Burgert, and G. Siqueira, Functionalized cellulose nanocrystals as active reinforcements for light-actuated 3d-printed structures, ACS Nano **16**, 18210 (2022).

[15] S. S. Ahankari, A. R. Subhedar, S. S. Bhadauria, and A. Dufresne, Nanocellulose in food packaging: A review, Carbohydr. Polym. **255**, 117479 (2021).

[16] X. Wang, J. Guo, H. Ren, J. Jin, H. He, P. Jin, Z. Wu, and Y. Zheng, Research progress of nanocellulose-based food packaging, Trends Food Sci. Technol. **143**, 104289 (2024).

[17] J.-F. Revol, L. Godbout, and D. Gray, Solid self-assembled films of cellulose with chiral nematic order and optically variable properties, J. Pulp Pap. Sci. **24**, 146 (1998).

[18] F. D'Acierno, K. Bakrani, W. Y. Hamad, C. A. Michal, and M. J. Maclachlan, Tuning the optical and thermal properties of both iridescent and colorless cellulose nanocrystal films, ACS Sustainable Chem. Eng. **10**, 8715 (2022).

[19] C. Williams, R. Parker, A. Kyriacou, M. Murace, and S. Vignolini, Inkjet printed photonic cellulose nanocrystal patterns, Adv. Mater. **36**, e2307563 (2023).

[20] G. Chu, F. Chen, B. Zhao, X. Zhang, E. Zussman, and O. J. Rojas, Self-assembled nanorods and microspheres for functional photonics: Retroreflector meets microlens array, Adv. Opt. Mater. **9**, 2002258 (2021).

[21] R. M. Parker, T. H. Zhao, B. Frka-Petesic, and S. Vignolini, Cellulose photonic pigments, Nat. Commun. **13**, 3378 (2022).

[22] Y. Geng, C. Honorato-Rios, J. Noh, and J. Lagerwall, Cholesteric spherical reflectors with tunable color from single-domain cellulose nanocrystal microshells, Adv. Mater. **36**, e2305251 (2023).

[23] F. Hennrich, R. Krupke, K. Arnold, J. A. Rojas Stütz, S. Lebedkin, T. Koch, T. Schimmel, and M. M. Kappes, The mechanism of cavitation-induced scission of single-walled carbon nanotubes, J. Phys. Chem. B **111**, 1932 (2007).

[24] Y. Y. Huang, T. P. J. Knowles, and E. M. Terentjev, Strength of nanotubes, filaments, and nanowires from sonication-induced scission, Adv. Mater. **21**, 3945 (2009).

[25] R. W. N. Nugroho, B. L. Tardy, S. M. Eldin, R. A. Ilyas, M. Mahardika, and N. Masruchin, Controlling the critical parameters of ultrasonication to affect the dispersion state, isolation, and chiral nematic assembly of cellulose nanocrystals, Ultrason. Sonochem. **99**, 106581 (2023).

[26] S. Beck, J. Bouchard, and R. Berry, Controlling the reflection wavelength of iridescent solid films of nanocrystalline cellulose, Biomacromolecules **12**, 167 (2011).

[27] B. Zakani, S. Entezami, D. Grecov, H. Salem, and A. Sedaghat, Effect of ultrasonication on lubrication performance of cellulose nano-crystalline (CNC) suspensions as green lubricants, Carbohydr. Polym. **282**, 119084 (2022).

[28] E. Gicquel, J. Bras, C. Rey, J. L. Putaux, F. Pignon, B. Jean, and C. Martin, Impact of sonication on the rheological and colloidal properties of highly concentrated cellulose nanocrystal suspensions, Cellulose **26**, 7619 (2019).

[29] M. Girard, F. Bertrand, J. R. Tavares, and M. C. Heuzey, Rheological insights on the evolution of sonicated cellulose nanocrystal dispersions, Ultrason. Sonochem. **78**, 105747 (2021).

[30] G. Nyström, M. Arcari, J. Adamcik, I. Usov, and R. Mezzenga, Nanocellulose fragmentation mechanisms and inversion of chirality from the single particle to the cholesteric phase, ACS Nano **12**, 5141 (2018).

[31] C. A. Maestri, M. Abrami, S. Hazan, E. Chistè, Y. Golan, J. Rohrer, A. Bernkop-Schnürch, M. Grassi, M. Scarpa, P. Bettotti, A. Bernkop-Schnürch, M. Grassi, M. Scarpa, and P. Bettotti, Role of sonication pre-treatment and cation valence in the sol-gel transition of nano-cellulose suspensions, Sci. Rep. **7**, 11129 (2017).

[32] X. Dong, J. Revol, and D. Gray, Effect of microcrystallite preparation conditions on the formation of colloid crystals of cellulose, Cellulose **5**, 19 (1998).

[33] S. J. Zhang, I. A. Kinloch, and A. H. Windle, Mesogenicity drives fractionation in lyotropic aqueous suspensions of multiwall carbon nanotubes, Nano Lett. **6**, 568 (2006).

[34] C. Honorato-Rios, C. Lehr, C. Schütz, R. Sanctuary, M. A. Osipov, J. Baller, and J. P. F. Lagerwall, Fractionation of cellulose nanocrystals: Enhancing liquid crystal ordering without promoting gelation, NPG Asia Mater. **10**, 455 (2018).

[35] C. Honorato-Rios and J. P. Lagerwall, Interrogating helical nanorod self-assembly with fractionated cellulose nanocrystal suspensions, Commun. Mater. **1**, 69 (2020).

[36] I. Usov, G. Nyström, J. Adamcik, S. Handschin, C. Schütz, A. Fall, L. Bergström, and R. Mezzenga, Understanding nanocellulose chirality and structure-properties relationship at the single fibril level, Nat. Commun. **6**, 7564 (2015).

[37] L. Onsager, The effects of shape on the interaction of colloidal particles, Ann. N. Y. Acad. Sci. **51**, 627 (1949).

[38] J. Araki and S. Kuga, Effect of trace electrolyte on liquid crystal type of cellulose microcrystals, Langmuir **17**, 4493 (2001).

[39] C. Schütz, J. R. Bruckner, C. Honorato-Rios, Z. Tosheva, M. Anyfantakis, and J. P. F. Lagerwall, From equilibrium liquid crystal formation and kinetic arrest to photonic bandgap films using suspensions of cellulose nanocrystals, Crystals **10**, 199 (2020).

[40] D. G. Gray, Order and gelation of cellulose nanocrystal suspensions: An overview of some issues, Phil. Trans. R. Soc. A **376**, 20170038 (2018).

[41] S. R. S. Veloso, A. G. Azevedo, P. F. Teixeira, and C. B. P. Fernandes, Cellulose nanocrystal (CNC) gels: A review, Gels **9**, 574 (2023).

[42] B. Frka-Petesic, G. Kamita, G. Guidetti, and S. Vignolini, Angular optical response of cellulose nanocrystal films explained by the distortion of the arrested suspension upon drying, Phys. Rev. Mater. **3**, 045601 (2019).

[43] H. See, M. Doi, and R. Larson, The effect of steady flow fields on the isotropic–nematic phase transition of rigid rod-like polymers, J. Chem. Phys. **92**, 792 (1990).

[44] A. Rey, Bifurcational analysis of the isotropic-nematic phase transition of rigid rod polymers subjected to biaxial stretching flow, Macromol. Theory Simul. **4**, 857 (1995).

[45] T. A. J. Lenstra, Z. Dogic, and J. K. G. Dhont, Shear-induced displacement of isotropic-nematic spinodals, J. Chem. Phys. **114**, 10151 (2001).

[46] R. Kádár, S. Spirk, and T. Nypelö, Cellulose nanocrystal liquid crystal phases: Progress and challenges in characterization using rheology coupled to optics, scattering, and spectroscopy, ACS Nano **15**, 7931 (2021).

[47] T. Gibaud, N. Dagès, P. Lidon, G. Jung, L. C. Ahouré, M. Sztucki, A. Poulesquen, N. Hengl, F. Pignon, and S. Manneville, Rheoacoustic gels: Tuning mechanical and flow properties of colloidal gels with ultrasonic vibrations, Phys. Rev. X **10**, 011028 (2020).

[48] C. Zakri, C. Blanc, E. Grelet, C. Zamora-Ledezma, N. Puech, E. Anglaret, and P. Poulin, Liquid crystals of carbon nanotubes and graphene, Philos. Trans. A Math Phys. Eng. Sci. **371**, 20120499 (2013).

[49] See Supplemental Material at http://link.aps.org/supplemental/10.1103/9rny-g949 for experimental video visualizing paranematic ordering during sonication. For full video caption, see Appendix G.

[50] H. Kneppe and F. Schneider, Viscosity, in *Handbook of Liquid Crystals Set* (Wiley, Weinheim, Germany, 1998), pp. 142–169.

[51] T. G. Parton, R. M. Parker, G. T. van de Kerkhof, A. Narkevicius, J. S. Haataja, B. Frka-Petesic, and S. Vignolini, Chiral self-assembly of cellulose nanocrystals is driven by crystallite bundles, Nat. Commun. **13**, 2657 (2022).

[52] M. Chiappini, S. Dussi, B. Frka-Petesic, S. Vignolini, and M. Dijkstra, Modeling the cholesteric pitch of apolar cellulose nanocrystal suspensions using a chiral hard-bundle model, J. Chem. Phys. **156**, 014904 (2022).

[53] C. Metzger, R. Drexel, F. Meier, and H. Briesen, Effect of ultrasonication on the size distribution and stability of cellulose nanocrystals in suspension: An asymmetrical flow field-flow fractionation study, Cellulose **28**, 10221 (2021).

[54] A. Lokanathan, A. Nykänen, J. Seitsonen, L. Johansson, J. Campbell, O. Rojas, O. Ikkala, and J. Laine, Cilia-mimetic hairy surfaces based on end-immobilized nanocellulose colloidal rods, Biomacromolecules **14**, 2807 (2013).

[55] S. Finner, T. Schilling, and P. van der Schoot, Connectivity, not density, dictates percolation in nematic liquid crystals of slender nanoparticles, Phys. Rev. Lett. **122**, 097801 (2019).

[56] T. Emeršič, K. Bagchi, S. Fitz, A. Jensen, P. F. Nealey, and J. J. de Pablo, Stable non-equilibrium structures in chiral nematics under microfluidic flow, J. Phys. Chem. B **128**, 11441 (2024).

[57] S. Munson-McGee, Estimation of the critical concentration in an anisotropic percolation network, Phys. Rev. B **43**, 3331 (1991).

[58] S. Finner, A. Atashpendar, T. Schilling, and P. van der Schoot, Unusual geometric percolation of hard nanorods in the uniaxial nematic liquid crystalline phase, Phys. Rev. E **100**, 062129 (2019).

[59] K. Ballu, J. Lim, T. Parton, R. Parker, B. Frka-Petesic, A. Lapkin, Y. Ogawa, and S. Vignolini, Tailoring the morphology of cellulose nanocrystals via controlled aggregation, ACS Nano **19**, 25228 (2025).

[60] https://zenodo.org/records/18673099.

[61] M. Reid, M. Villalobos, and E. Cranston, Benchmarking cellulose nanocrystals: From the laboratory to industrial production, Langmuir **33**, 1583 (2017).

[62] https://en.wikipedia.org/wiki/Sturges%27s_rule.